

MEDICALNARRATIVES: Connecting Medical Vision and Language with Localized Narratives

Wisdom O. Ikezogwo * Kevin Zhang *
 Mehmet Saygin Seyfioglu Fatemeh Ghezloo Linda Shapiro Ranjay Krishna
 University of Washington

Abstract

We propose MedicalNarratives, a dataset curated from medical pedagogical videos similar in nature to data collected in Think-Aloud studies and inspired by Localized Narratives, which collects grounded image-text data by curating instructors’ speech and mouse cursor movements synchronized in time. MedicalNarratives enables pretraining of both semantic and dense objectives, alleviating the need to train medical semantic and dense tasks disparately due to the lack of reasonably sized datasets. Our dataset contains 4.7M image-text pairs from videos and articles, with 1M samples containing dense annotations in the form of traces and bounding boxes. To evaluate the utility of MedicalNarratives, we train GENMEDCLIP based on the CLIP architecture using our dataset spanning 12 medical domains and demonstrate that it outperforms previous state-of-the-art models on a newly constructed medical imaging benchmark that comprehensively evaluates performance across all modalities. Data, demo, code and models available at <https://medical-narratives.github.io/>

1. Introduction

Analyzing medical images is an intrinsically perceptual and conceptual task [86] requiring the expert to extract visual clues from the imaging modalities and to conceptually retrieve knowledge from memory and utilize his/her understanding to lead to a diagnosis. This cognitive process requires connecting spatial regions of the image to clinical understanding, often utilizing a segmental approach to avoid errors. This makes reading and communicating medical imaging information, and innately dense and semantic task requiring understanding and grounding.

Within medical image analysis today, studies on semantic tasks like classification, captioning, and retrieval are typically explored separately from dense tasks like segmentation, detection, and disease monitoring, this can be attributed to the lack of the model architecture that enables exploring both

fields of research in tandem, and the lack of datasets to train such models natively. This problem is not unique to medical image analysis; in the general domain this dichotomy exists, even with the similar underlying Transformer architecture [126] model architectures like CLIP [57, 102] perform well on semantic tasks and models like DINO [21] outperform on dense tasks. Recently, there has been active research into developing methods that can perform both types of tasks [42, 76, 84, 100, 138], supported by datasets that contain images, spatial annotations, and the language to connect them [71, 100].

While the cost to collect these datasets can be steep, certain annotation protocols strike a good balance between ease of collection, and utility. Specifically, Localized Narratives [100, 128], proposed a dataset of image, text, and grounding traces. They did this by having annotators describe an image vocally while simultaneously moving a computer mouse to the regions they describe, resulting in holistic descriptions of the scene/image all grounded in real-time with regions of the image, capturing both semantic understanding of the scene and object relations. This protocol of collecting grounded vision-language (VL) datasets does not have strict spatial annotations yet captures strong spatial correlations to the description with every trace, making the protocol uniquely easier to undertake and capture data en mass as it appeals to the human nature to point while describing a scene [46, 61, 129]. Localized narratives have been used to train models on semantic tasks [100, 128, 139], dense tasks [33, 39, 42] and more recently to train generative multimodal language models (MLLM) like PixelLM [134], Quilt-LLaVA [118], and Molmo[32] and other generative image models [69, 136].

Unlike the general domain with web-scale datasets [117] and performative models that translate into products, medical foundational and generative models do not translate well into clinical use. While a major reason is the heightened level of sensitivity and slow adoption, we argue the lack of naturally aligned multimodal data that scales with model parameterization is also a major contributing factor. Recent work like MedTrinity-25M [133], attempts to address this by releasing a multimodal dataset with spatial annotations,

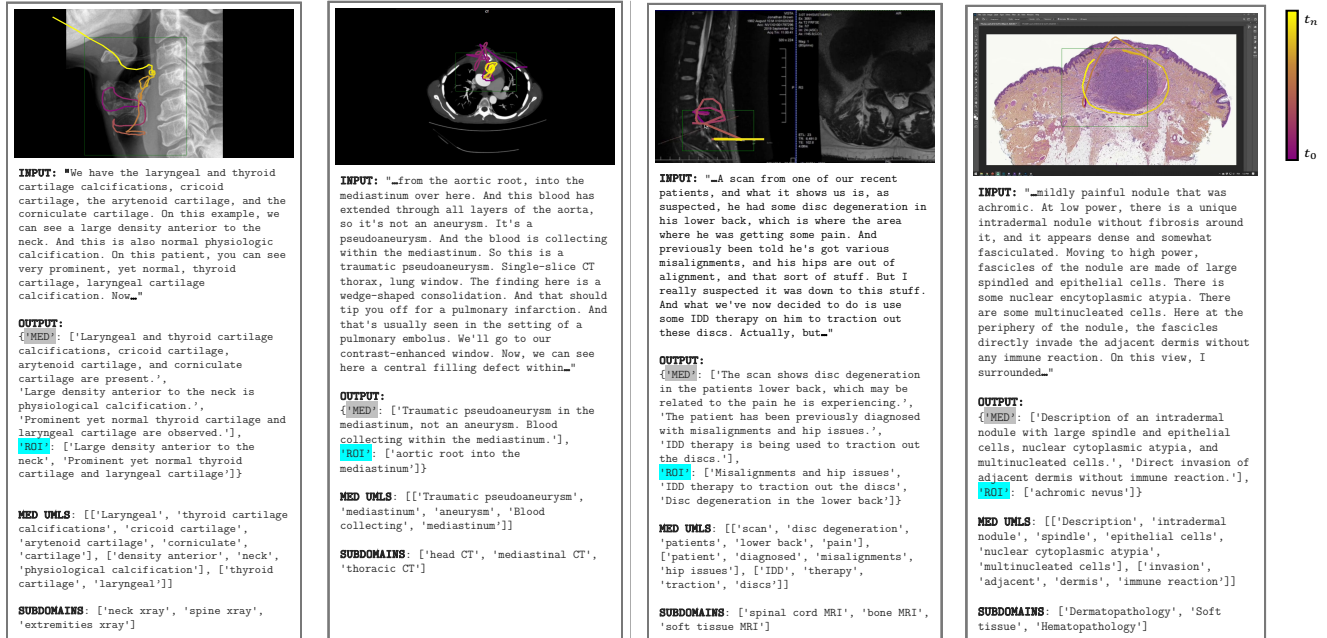


Figure 1. **MEDICALNARRATIVES:** Here we show 4 samples from the dataset, these samples come from varying videos containing 4 medical modalities, **X-ray, CT, MRI, and Histopathology** images from left to right. These samples are selected from interleaved samples extracted from source videos, with each sample showing the representative image captured, the raw input text grounded and aligned in-time with the spatial traces & bbox, the denoised medical and ROI text describing the medical image removing all transcription errors, and non-medical information. Please see more examples across all 4 modalities we capture **MEDICALNARRATIVES** for in the Appendix.

but relies on sub-optimally pretrained models to generate text descriptions and Regions of Interests (ROIs) for medical images lacking ground truth annotations, potentially propagating model biases and errors.

To address these limitations, we draw inspiration from how medical experts naturally communicate and teach. In the joint field of cognitive psychology and medical imaging, studying how medical experts analyze patient data, studies leverage the think-aloud protocol [35] to capture data for various types of analysis. Within this protocol, experts verbalize their thoughts as they perform a task, and in certain studies they capture their eye gaze/cursor localizing the regions of the image on which they focus [49, 75]. This protocol has been used to collect some medical datasets [85, 96] including the Tufts dental x-ray database [96] which captures a multi-modal dataset including the radiologist’s expertise captured in the form of eye-tracking and think-aloud protocol.

Following this intuition and building upon prior work Quilt-LLaVA [118], we propose **MEDICALNARRATIVES** a dataset that leverages pedagogical medical videos where instructors naturally narrate descriptions while pointing to relevant regions with their cursor - closely mimicking the think-aloud protocol used in clinical practice. Our dataset contains 4.2M image-text pairs across 11 medical modalities and 1 pseudo-medical domain, with interleaving samples

between varying modalities (e.g., X-ray and CT for the same patient). Importantly, 875K of these samples are grounded in traces that can be reformatted into bounding boxes or masks, serving to train various tasks including dense models like MedSAM [24, 81] while being flexible for extension in clinical settings with minor adjustments to current diagnostic workflows.

To test the utility of our models we train a vision-language model called **GENMEDCLIP** on our dataset and evaluate it on a new benchmark of datasets that cut across all 11 medical modalities for both classification and retrieval where we see **GENMEDCLIP** outperform prior SOTA models like **BIOMEDCLIP** in both tasks with 3% and 14% respectively. We hope future works leverage the dataset to train more grounded generative models similar to Quilt-LLaVA [118], LLaVA-Med++ [133], and PixelLLM [134] as well as open-vocabulary segmentation/detection models. To bolster other use cases we also release the constituting video clips and many other metadata including UMLS entities.

2. Related work

2.1. Vision Language representation

Vision-language (multi-modal) models have evolved over time in both supervised and self-supervised paradigms;

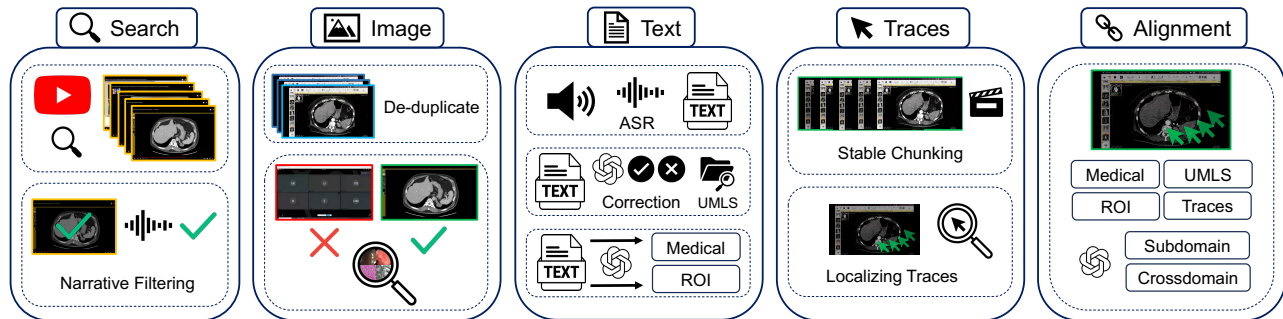


Figure 2. The data curation pipeline for the Video subset of the MEDICALNARRATIVES dataset. **Search:** YouTube video-first search strategy, with filtering by pre-trained classifiers and heuristics. **Image:** Extracting keyframes of a video, denoising, and identifying medical images. **Text:** ASR transcription, text correction with LLMs, and medical/ROI text extraction. **Traces:** Identifying stable chunks of a video, then localizing cursor traces within each chunk. **Alignment:** Mapping medical/ROI text, traces, and images together. Samples are classified into finer-grained subdomains and samples with discussions of multiple domains are identified with LLMs.

in recent studies, contrastive self-supervision objectives [57, 102, 141] that learn by matching paired-modality embeddings have outperformed prior work [26, 74, 79] in downstream tasks and, more importantly, perform better at zeros-shot tasks or on emergent domains for which disparate modalities share a paired domain [40, 145]. In medical imaging, early studies in radiology [51, 141] were pre-trained on specific x-ray images and their reports, and more recently domain specific VL models have pushed the SOTA on various tasks with models developed for Ophthalmology [119], Histopathology [52, 54], Computed Tomography [48], Mammography [25], Dermatology [68], Ultrasound/Echocardiography [27]. These models work well for the specific domains they are trained on and not for other domains, which may not have enough data to train for, hence the push for more general medical models [124, 140, 144].

2.2. Medical (Localized) Narratives

In training these VL models, much research effort is used in sourcing, filtering, and curating medical image(s)-text(s) paired data for pre-training, mostly sourcing general and specific medical domain datasets from Medical reports [60], PubMed [36, 37, 109, 140], books [37], social-media [52, 54], YouTube/videos [54, 118] or mixtures of these [133]. The utilization of these data for dense tasks like segmentation and detection (open-closed vocabulary) is limited as they do not provide any spatial annotation localizing regions of the images to specific labels/text. In contrast, every word in a localized narrative [100, 118, 128, 139] is grounded to a region of the representative image by the point/trace captured. This datasets have been used to train models for semantic reasoning [100, 128, 139], and for dense tasks [33, 39, 42], and they also support training both generative multimodal language models [118, 128, 134] and generative image models [69, 136]. Specifically in medi-

cal image analysis, Quilt-LLaVA [118] adopts this paired data structure for training its histopathology chatbots with improved spatial reasoning, and PathNarrative’s [139] hierarchical decision-to-reason localized narrative structure, enables classification and captioning tasks, while providing explainable clues for clinicians to understand and diagnose, improving human-AI collaboration in diagnosis.

3. MEDICALNARRATIVES: Curation, Formatting, and Characterization

3.1. Overview

Curating a vision-language dataset with spatial traces from unstructured pedagogy videos is a non-trivial, as many videos either lack voiced audio, are not in English, fail to contain medically relevant content, or have insufficient medical relevance—for example, present static images of medical content on a slide deck, or briefly cover medical images in pursuit of a different objective. In addition, conventional automatic speech recognition (ASR) systems also struggle with the specialized requirements of medical language transcription, necessitating a non-trivial solution. The de-noising of text and image modalities adds further complexity as the videos are typically conversational and, therefore, inherently noisy. Instructors often record both relevant and irrelevant visual content in their videos, making extracting frames at static intervals non-representative of the medical data contained in the video. To collect MEDICALNARRATIVES, we trained models and handcrafted algorithms that leverage the nuances in the instructors’ textual and visual behavior, ensuring accurate collection and alignment of both modalities.

3.2. Sourcing and Filtering Medical Data from PubMed and Videos

The MEDICALNARRATIVES curation pipeline expands on methods outlined in Quilt-1M [54] and Quilt-LLaVA [118]. It involves (a) sourcing video/article data across 12 medical imaging domains, (b) filtering videos/articles, (c) denoising the captured images, captions, and trace modalities, and (d) aligning all modalities.

3.2.1 Collecting representative videos and articles.

Videos: We first search for relevant channels and videos on YouTube, focusing on the 12 medical imaging domains including: Magnetic Resonance Imaging (MRI), X-Rays, Computed Tomography (CT), Ultrasound (US), Mammography (Mammo), Surgery (Surg), Endoscopy (Endo), Dentistry, Dermatology, Ophthalmology (Ophtha), Histopathology (Histo), and General Medical Illustrations. Using keywords collected for each outlined domain (see section 7.1 in the Appendix), we search for relevant videos to expedite discovery and exploit found videos by then searching through the corresponding channel for more relevant videos. Once identified, we download low-resolution versions of the videos for filtering.

Articles: We download article documents from the PubMed Central Open Access Subset (PMC-OA) [90], which contains 5.47M articles. We then process each article, extracting figures and captions. We also search for inline references to figures within the body of an article to add to each figure-caption data pair.

3.2.2 Filtering for narrative medical videos and relevant article samples.

Videos: We modify filtering heuristics set by Quilt-1M to translate to other medical domain videos. These modified heuristics include: excluding videos shorter than 1 minute in duration or longer than 2 hours, non-voiced videos, and videos from channels with more than 1M subscribers. Next, we automatically identify relevant videos by extracting key-frames (frames containing significant visual changes from previous frames) from a video and using pre-trained classifiers to classify each key-frame. We set specific thresholds per-domain for minimum amount of visual change required to trigger a key-frame, since each modality is intrinsically different e.g. X-rays tend to be static images, while ultrasounds tend to be short repeating video clips (See section 7.2 in the Appendix). Finally, we identify narrative-style videos. For static domains (CT, X-ray, MRI), we select key-frames predicted to be medical and extract the next three (3) key-frames, computing the cosine similarity between the selected frame and each of the subsequent three frames. If all three have similarity scores \geq a preset threshold of 0.9, we

count it as a narrative streak. A video is tagged as narrative if a domain-specific preset percentage (%) of the selected frames exhibit a narrative streak. For non-static domains like ultrasound, we utilize the video’s transcript to look for speech around key-frames. A video is considered narrative if more than half the key-frames have text for more than a domain-specific number of seconds. Consequently, we download all narrative-style videos at full resolution.

Articles: Since these articles/studies are carefully written and reviewed, we inherit the benefit of this data source being inherently filtered and well curated by authors and reviewers of the constituent journals and simply classify each figure into one of the 12 medical imaging domains.

3.2.3 Text Extraction and Denoising.

Videos: In line with Quilt-1M [54] we leverage an open-source ASR model - Whisper [103] to transcribe all speech from the selected videos, making sure to account for transcription errors using a similar methodology of finding these types of errors and correcting with a language model. See section 7.4 in the appendix for further details of the error-extracting algorithm, medical n-gram verifier, and methodology behind leveraging a general-purpose LM for error correction.

Articles: Similarly we parse each article’s XML document, extracting each figure’s caption and inline mentions. Since many sub-figures are typically grouped into single large figures, we split the compounded figure captions into sub-captions, leveraging a language model to find and split sub-captions due to the non-triviality of identifying enumerations in the text and splitting the captions. Furthermore, we refine the inline mentions of a figure and match them to specific sub-captions/sub-figures; please see more details of this pairing in sections 8.1 8.4 and 8.6.

3.2.4 Image Extraction and Denoising.

Videos: For each video, we identify medical key-frames and subsequently leverage these frames’ times to split the video into time-intervals called *chunks* from which to extract representative image(s). To extract representative image(s), we use the median image (pixel-space) of stable (static) frames in each chunk if they exist, else we de-duplicate the captured key-frames, exploiting the human tendency in pedagogy videos to pause while explaining and pointing [46, 100, 118].

Articles: For scientific documents, we extract the figures as images. However, many of these figures contain multiple sub-figures, which can take nonconventional grid shapes and are labeled irregularly making the task of splitting into sub-figures and pairing with the correct sub-caption non-trivial. Since most compound figure layouts are not uniform and vary in the whitespace in between sub-figures, we train

an object detection model based on the YOLO architecture [59] on sub-figure annotation datasets MedICaT and ImageCLEF 2016 [38, 122]. See more details in section 8.3 of the appendix including examples of non-trivial cases.

3.2.5 Extracting Localizing Traces

Extracting the narrative traces/cursor location from medical clips poses a significant challenge due certain in-domain issues including homogeneity in color and texture, significant black/white background, alongside the presence of other dynamic elements in videos, such as minor pixel variations and variations in the narrators’ cursor movement speed and style; hence, we adopt the methodology proposed by QuiltLLaVA [118] centered around the observation that narrators typically pause before signaling with their cursor, guiding the audience’s attention to specific relevant regions while describing those regions. This allows us to isolate segments in each video where the background is mostly static, termed stable chunks. To detect the stable chunks, we develop a frame-differencing approach to detect chunks with minimal background movement. Our algorithm computes the absolute difference between consecutive frames and then applies a Gaussian filter for adaptive thresholding to detect frames with minor changes.

Given the homogeneity in medical images and backgrounds, this naive pixel-wise difference algorithm yields a high rate of false positives, namely, chunks that had a change occur in them are identified as stable. To alleviate this, we incorporate a perceptual metric, by evaluating the structural similarity index measure (SSIM) on randomly sampled patches to further verify whether a change has occurred between two frames.

Next, for each stable chunk where the background remains consistent, we calculate a median frame in the pixel domain to represent the background. This median frame is then subtracted from the frames within the stable chunk, and a threshold is applied to mitigate noise or other artifacts, effectively isolating the cursor. Subsequently, we capture the cursor by identifying the coordinates of the maximum pixel value. However, this approach assumes the absence of other slight movements with respect to pixel changes, which is not always the case, as there may be movements like the narrator’s facial expressions within the scene. We address this by applying a face detection model [115] to mask such distractions, ensuring our analysis concentrates solely on cursor movement. This algorithm offers a surprisingly generalizable way to collect cursor traces from any medical video in static domains like X-rays and histopathology. Finally, we extract the smallest bounding boxes around the traces.

3.3. Aligning modalities

Videos: Following prior work [54], to align image, text, and trace modalities we compute time chunks for each video denoted as $[(t_1, t_2), (t_3, t_4), \dots (t_{n-1}, t_n)]$ from key-frames after discriminating for medical frames using the pretrained classifiers – (*scene_chunks*). Each *scene_chunk* is padded with *pad_time* to its left and right. We use the methods described above to extract the medical/ROI captions as well as the representative image(s) for every chunk/time-interval in *scene_chunks*. Finally, each chunk in *scene_chunks* is mapped to text (both medical and ROI captions), traces and images. Next, we map each medical image to one or more medical text (with traces). Using the time interval in which the image occurs, we extract its raw text from ASR, then extract and correct keywords using the Rake method, which we refer to as *raw_keywords*. We extract keywords from each medical text returned using the LLM, and we refer to these as *keywords*. Finally, if the *raw_keywords* occur before or slightly after a selected representative image, and overlap with the *keywords* in one of the Medical/ROI texts for that chunk, we map the image to the medical/ROI text. Traces are encoded as the cartesian position of the cursor relative to the image size, we use (x_j^t, y_j^t) , where $x \in [0, W]$ and $y \in [0, H]$, with W and H representing the image width and height, respectively, t spans from 0 up to the total duration of the j^{th} stable chunk.

Articles: The majority of our curated PubMed data uses alphabetic labels in compound figures to denote sub-figures, which increases the complexity of pairing individual sub-figures from compound figures to sub-captions. Our solution leverages an optical character recognition (OCR)¹ on each sub-figure to detect the sub-figure labels, which we then match to the extracted sub-caption labels. To improve the reliability of this approach, we upscale the detected sub-figures by a factor of 4 to enlarge the sub-figure text label for OCR. We also impose a 95% confidence threshold on predicted text to isolate the sub-figure label, as text detected at lower confidence is often non-label text present in the figure (e.g. axis titles, graphs). We then attempt to match the detected sub-figure label with the sub-caption label. If a match is found, we pair the selected sub-figure and sub-caption. Despite the generality of this approach, we identified a few failure cases and proposed an error handling solution for these cases in section 8.5 of the appendix.

3.4. Characterizing MEDICALNARRATIVES

To create MEDICALNARRATIVES we combine medical narratives curated from videos with image-text pairs curated from PubMed, resulting in 4.7M total image-text samples of which 1M samples are localized narratives.

¹<https://github.com/JaidedAI/EasyOCR>

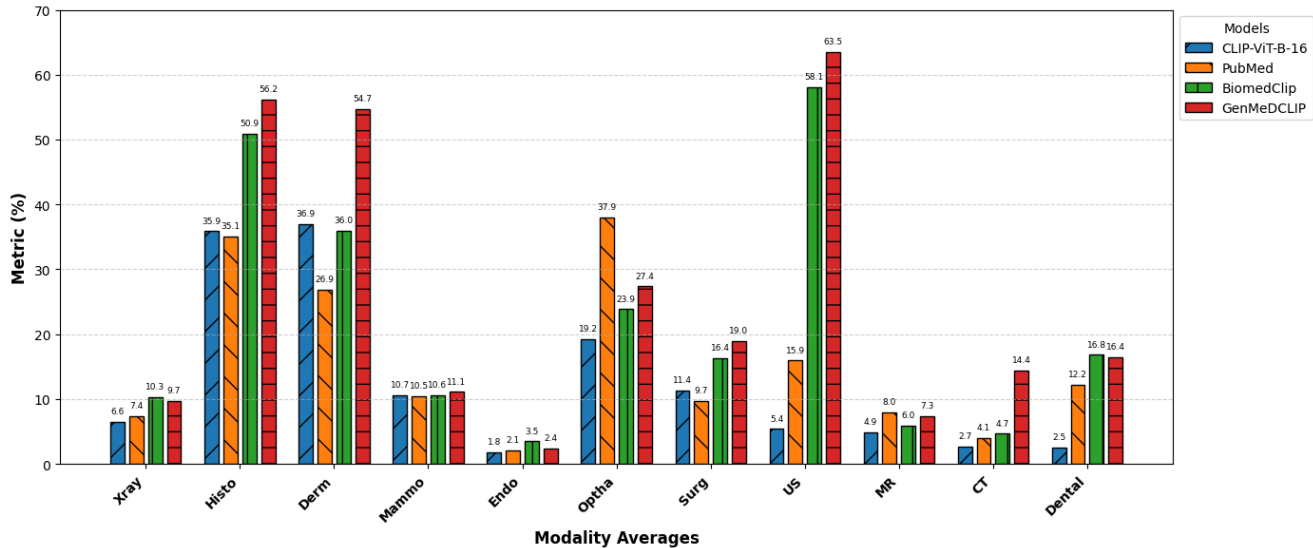


Figure 3. **Zeroshot Classification Results** shows that our model GENMEDCLIP outperforms all other baselines including the out-of-domain CLIP, and biomedical vision-language models BIOMEDCLIP, and PUBMEDCLIP across the constructed medical benchmark which covers all 11 medical domains represented. The metric for Xray and Mammography is mean average precision while the rest is accuracy.

3.4.1 Narratives

We searched over 738K videos and extracted 74K narrative-styled videos that passed our heuristics and had relevant medical imaging pedagogy, a 10.1% yield making up a total of 4526 hours of video. In total, we collect 809K unique images with an average size of H: 1521px and W: 903px and 1.62M image-text pairs from videos with 1M of these samples grounded with traces, these samples cover 101.6M number of unique trace points yielding 546K number of unique bounding boxes with an average size of H: 291px and W: 357px across the 4 domains with traces: CT, MRI, X-ray, and Histopathology. The mean length of the text captions is 22.37 words, with an average of 1.88 medical sentences per image. Our dataset spans over 4M UMLS entities from those mentioned in the text with over 300K unique entities across medical (e.g., findings, or disease) and non-medical (e.g., governmental or regulatory activity) semantic types.

3.4.2 Non-Narratives

We extract 5.4M articles from PubMed [90], with 23M figures, after filtering for medical figures only, we obtain 1.03M figures from 273K articles, and after sub-figure separation, we have an average of 2.62 subfigure-subcaption pairs per-article figure, with an average of 45.45 words per-caption.

3.5. Quality

Unlike localized narratives [100, 128] where localization accuracy can be measured by comparing against human annotation, none of our videos to our knowledge have any

structured human spatial annotation to compare against. Nonetheless, to evaluate our pipeline’s performance, we assess several aspects. First, we calculate the precision of our LLM’s corrections by dividing the number of conditioned misspelled errors replaced (i.e., passed the UMLS check) by the total number of conditioned misspelled words found, yielding an average of 47.99%. We also determined the unconditioned precision of the LLM, similar to the previous step, and found it to be 17.58%. Therefore, we replace our detected incorrect words with the LLM’s correction 47.99% of the time, and 17.58% of the time we replace the LLM’s detected errors with its correction. To estimate the ASR model’s transcription performance, we compute the total number of errors replaced (both conditioned and unconditioned) and divide it by the total number of words in each video, resulting in an average ASR error rate of 0.81%. Also note that, by prompting the LLM to extract only medically relevant text, we further eliminate identifiable information, such as clinic addresses, from our dataset.

4. GENMEDCLIP: Experiments and Results

Since MEDICALNARRATIVES supports semantic tasks, we test the utility of our dataset on two medically relevant tasks image classification (zeroshot and linear probing) and cross-modal information retrieval (zero-shot) across all in-domain modalities. We select the Contrastive Language-Image Pre-training (CLIP) objective [102] to pre-train a VL model we call GENMEDCLIP. We train several models, varying the image and text encoders and making adaptations inline with prior work on the choice of encoders and text tokenization

for improved performance [54, 140]. For the image tower we finetune Vision Transformers (ViT-Base) [34] models pre-trained using a supervised cross-entropy objective (ViT-Base-16 and ViT-Base-32 [132]) and unsupervised contrastive objective ViT-Base-16) [102], on 224*224 pixel images. On the text tower, we use GPT2 [101] with a context length of 77, and BioMedBert [45] with context size to 256. To train our models we utilize the open-source implementation of CLIP [102] called OpenClip [55] on 4 Nvidia A40 GPUs for 20 iterations over the entire train dataset of 4.2M samples. To ensure a fair comparison with baselines we trained three different variants of our model: GENMEDCLIP-32: with ViT-B/32 image-tower with GPT2/77 text-tower architecture, GENMEDCLIP-PMB: with ViT-B/16 image-tower and Bert/256 BiomedBert [45] text-tower architecture, and GENMEDCLIP-PMB: with ViT-B/16 image-tower with GPT2/77 [45] text-tower architecture; all finetuned for 20 epochs over our train-set. Please see training hyperparameters used in Section 10 of the Appendix.

Model	Isic	Til	Pcam	Mhist	Nck	Mammo	Avg
CLIP-ViT-B-16 [102]	71.23	91.23	82.42	63.97	92.26	83.30	80.74
PUBMEDCLIP [36]	68.58	91.32	84.07	72.16	92.29	83.90	82.06
BIOMEDCLIP [140]	68.25	91.82	83.43	66.73	93.05	83.70	81.17
GENMEDCLIP-32	72.75	93.26	86.77	72.06	92.77	83.70	83.55
GENMEDCLIP-PMB	69.38	91.51	84.54	67.66	88.02	84.20	80.88
GENMEDCLIP	74.87	93.34	87.69	72.16	90.84	84.90	83.97

Table 1. **Linear Probing** results across datasets representing Dermatology (Isic), Histopathology (pcam, mhist, nck), and Mammography (vinDr-Mammo) classification tasks. GENMEDCLIP outperforms all baselines showing the capacity of our model to be fine-tuned for downstream tasks. The metric used is accuracy.

4.1. Benchmarking on Downstream Medical Tasks

We evaluate the utility of GENMEDCLIP on a new medical imaging benchmark of all medical domains represented in our pre-training dataset MEDICALNARRATIVES, with some domains represented by ≥ 1 dataset/task for classification, totaling 29 downstream datasets and on a held-out set of 1000 unique images for the retrieval task downstream. For MRI we use the **RadImageNet** [83] MRI subsets tasks based on the anatomical region scanned in the image these include Ankle/foot with 25 classes, Brain with 10 classes, Knee with 18 classes, Abdomen/pelvis with 26 classes, Hip with 14 classes, Shoulder with 14 classes, Spine with 9 classes. To evaluate on CT domain we also use RadImageNet’s [83] CT dataset which cover two (2) anatomical regions with Lung having 6 sub-classes and Abdomen/pelvis with 28 subclasses. For ultrasound, we evaluate on RadImageNet’s [83] US dataset which covers a total of 15 classes across Thyroid and Abdomen/pelvis anatomical regions. For Xray, we evaluate on **VinDr-CXR** Chest Xrays [91] test set and report the mean

average precision (mAP) across all 28 findings, similarly to evaluate on Mammography we use **VinDr-Mammo** [92] and report the mAP on all X findings, leveraging only the standard bilateral craniocaudal (CC) view of the test set. We evaluate on surgical organ classification using **Dresden** [22] which covers 8 abdominal organs; to evaluate for endoscopy domain we test on all procedures images in **GastroVision** [56] with 27 classes. For Dermatology we evaluate on the **Diverse Dermatology Images** (DDI) [31] binary (benign or malignant) dataset and Isic 2018 dataset [28]. For Dentistry we evaluate on **Dental orthopantomography** (OPG) [104] X-ray dataset with 6 classes. To evaluate the Ophthalmology domain we evaluate on **G1020** [13] a retinal fundus glaucoma dataset and on **Optical Coherence Tomography Dataset** (OCTDL) [72] with 6 disease classes. We evaluate the Histopathology domain on the following datasets: **Patch-Camelyon** [127] for lymph node metastatic tissue binary prediction task, **NCT-CRC-HE-100K** [63] on 8 morphological classes, **BACH** [10] which consists of breast tissues with 4 classes including benign and invasive carcinoma, **Osteo** [12] osteosarcoma dataset with 3 classes including necrotic tumor, **SkinCancer** [70] dataset of tissue patches from skin biopsies of 12 anatomical classes and 4 neoplasm categories that make up the SkinTumor Subset, we also evaluate on **MHIST** [131] dataset of colorectal polyps tissue, **LC25000** [18] dataset, which is split in-between LC25000 (Lung) and LC25000 (Colon), for lung and colon adenocarcinomas classification, and on TCGA-TIL [113] for tumor-infiltrating lymphocytes (TILs) binary classification, based on H&E images from 13 of The Cancer Genome Atlas (TCGA) tumor types.

Models	T2I retrieval			I2T retrieval			Avg
	@5	@50	@200	@5	@50	@200	
CLIP-ViT-B-16 [102]	3.48	20.38	35.69	3.56	20.39	35.42	19.82
PUBMEDCLIP [36]	1.44	12.68	25.44	1.10	12.30	24.07	12.84
BIOMEDCLIP [140]	16.50	51.48	67.46	15.71	48.85	64.61	44.10
GENMEDCLIP-32	22.36	76.33	88.60	20.75	75.15	88.23	61.90
GENMEDCLIP-PMB	28.29	82.91	92.43	29.21	82.91	92.43	68.03
GENMEDCLIP	34.89	83.83	92.27	34.26	83.48	92.32	70.17

Table 2. **Retrieval** results on our held-out set of 16K samples across all medical domains, show that our model GENMEDCLIP outperforms all other baselines on both Zeroshot image-to-text and vice-versa text-to-image retrieval task.

4.2. Zero-shot classification

A model must maintain a comprehensive understanding without requiring specific data for retraining. Thus, we evaluate our model’s zero-shot performance against three state-of-the-art models: CLIP, BIOMEDCLIP, and PUBMEDCLIP. In Figure 3, each domain in the benchmark is represented by a set of datasets (as provided above). The prompts used

for these evaluations are presented in Table 6 in the Appendix. Across the benchmark our model average the following GENMEDCLIP-32: 31.33%, GENMEDCLIP-PMB: 31.46%, and GENMEDCLIP: 32.55% metric all outperforming BIOMEDCLIP with 27.80 overall by a max value of 4.75%. Specifically, as shown in Figure Fig. 3, GENMEDCLIP outperforms all baselines in 5 medical domains: Histopathology, Dermatology, Mammography, Surgery, Ultrasound, and CT. GENMEDCLIP is also comparable to baselines in the Chest X-ray, Endoscopy, Ophthalmology, and MRI domains.

4.3. Supervised linear probing

We assess the full-shot performance of our model by conducting linear probing with 100% of the training data; we report the average accuracy over all benchmark evaluation across five distinct datasets, specifically those with dedicated training and testing sets among our external datasets in Dermatology, Histopathology, and Mammography. Remarkably, our model, utilizing the ViT-B/32 architecture with GPT/77, outperforms its counterparts, BIOMEDCLIP, and CLIP, in most datasets. Overall, on average GENMEDCLIP outperforms all other models including BIOMEDCLIP and PUBMEDCLIP with over 2.8%, and over 1.9% respectively.

4.4. Cross-Modal Retrieval

We evaluate cross-modal retrieval performance by examining both zero-shot text-to-image and image-to-text retrieval capabilities. To do so we leverage a randomly selected held-out partition of MEDICALNARRATIVES, not used in training our models. The held-out set contains 16K image-text pairs with the following medical modality distribution: 1756 X-ray, 1237 MRI, 1851 CT, 1351 Ultrasound, 1744 Surgery, 1346 Endoscopy, 1189 Dermatology, 1216 Dentistry, 1151 Ophthalmology, 1000 Histopathology, 1299 General Medical, 1149 Other (Mammo etc) image-text pairs. We conduct retrieval, in our study, by identifying the nearest neighbors for each modality and then determining whether the corresponding pair is within the top N nearest neighbors, where $N \in \{1, 50, 200\}$, mimicking several medical search tasks. Results in Table 2 shows that on average GENMEDCLIP outperforms all baselines and specifically outperforms BIOMEDCLIP by 26.07%, The results also confirm the observation made in BIOMEDCLIP [140] where the general CLIP model outperforms the in-domain model PUBMEDCLIP by 6.98%

5. Conclusion

In this work, we propose a robust protocol for annotating medical narratives, aiming to standardize the process of constructing multimodal medical datasets. Our curated dataset MEDICALNARRATIVES, which follows the Narratives Annotation Protocol addresses the specific challenges of medical data collection at scale balancing the relationship between

utility and ease/cost of collection. We argue that this protocol can serve as the de facto standard for annotating future multimodal medical datasets, particularly given its flexibility in capturing grounded text describing medical images effectively. By establishing and scaling this protocol, we pave the way for systematic and scalable dataset creation for all medical domains.

For semantic tasks, we demonstrate a strong performance over prior vision-language (VL) models on our well-curated medical imaging benchmark, across both classification (zero-shot, and full-shot) and retrieval tasks, establishing new VL state-of-the-art results and demonstrating the effectiveness of in-domain data filtration methods on model performance, as we finetune our GENMEDCLIP on 4.7M samples while BIOMEDCLIP trains on over 15M samples. We hope future work leverages our developed models, dataset, and protocol.

6. Limitations

While our approach and findings contribute significantly to the development of multimodal medical datasets and model performance in the medical domain, certain limitations need to be acknowledged:

- Underlying Bias in Abnormality Representation:** A major drawback in our dataset is its overrepresentation of abnormal cases, a bias that mirrors reality as in hospitals, diagnostic imaging is typically performed only after significant clinical suspicion of pathology. Consequently, our data disproportionately captures abnormal findings, which may affect the model’s generalizability to balanced populations and lead to bias in clinical decision support.
- Focus on 2D Medical Imaging:** Our work is limited to 2D medical images, despite the prevalence of 3D imaging modalities (such as MRI, CT, and OCT scans). While recent studies suggest that 2D approaches can sometimes rival or surpass native 3D approaches, there remain applications where 3D data could offer distinct advantages. Expanding our dataset and methodology to include 3D imaging would be an important step toward broader applicability and model performance.
- Exclusion of Other Medical Data Modalities:** This work currently focuses solely on medical imaging data, excluding other critical types of medical data such as laboratory tests, time-series signals, genetic data, and patient histories. These additional data sources are valuable for building comprehensive and holistic patient models, and their integration is key for achieving the goal of generalist medical models [124, 144].
- Lack of Localization Accuracy:** Our dataset does not contain direct human-annotated ground truth for localization, such as bounding boxes that indicate the specific regions associated with the text. This limitation impacts our ability to measure the overlap between trace annotations collected from videos and human annotations.

References

- [1] Glaucoma detection. <https://www.kaggle.com/datasets/sshikamaru/glaucoma-detection>. 29
- [2] Ocular disease recognition. <https://www.kaggle.com/datasets/andrewmvd/ocular-disease-recognition-odir5k>. Ocular Disease Recognition — Kaggle. 29
- [3] Mahmoud Afifi. 11k hands: Gender recognition and biometric identification using a large dataset of hand images, 2018. 29
- [4] Walid Al-Dhabyani, Mohammed Gomaa, Hussien Khaled, and Aly Fahmy. Dataset of breast ultrasound images. *Data in Brief*, 28:104863, 2020. 29
- [5] B. Albertina, M. Watson, C. Holback, R. Jarosz, S. Kirk, Y. Lee, K. Rieger-Christ, and J. Lemmerman. The cancer genome atlas lung adenocarcinoma collection (tcga-luad) (version 4), 2016. 29
- [6] Hassan ALHAJJ, Mathieu Lamard, Pierre-henri Conze, Béatrice Cochener, and Gwenolé Quéllec. Cataracts, 2021. 29
- [7] A. Alhudhaif, Z. Cömert, and K. Polat. Otitis media detection using tympanic membrane images with a novel multi-class machine learning algorithm. *PeerJ Comput Sci*, 7:e405, 2021. 29
- [8] Michela Antonelli, Annika Reinke, Spyridon Bakas, Keyvan Farahani, Annette Kopp-Schneider, Bennett A. Landman, Geert Litjens, Bjoern Menze, Olaf Ronneberger, Ronald M. Summers, Bram van Ginneken, Michel Bilello, Patrick Bilic, Patrick F. Christ, Richard K. G. Do, Marc J. Gollub, Stephan H. Heckers, Henkjan Huisman, William R. Jarnagin, Maureen K. McHugo, Sandy Napel, Jennifer S. Golia Pernicka, Kawal Rhode, Catalina Tobon-Gomez, Eugene Vorontsov, James A. Meakin, Sebastien Ourselin, Manuel Wiesenfath, Pablo Arbeláez, Byeonguk Bae, Sihong Chen, Laura Daza, Jianjiang Feng, Baochun He, Fabian Isensee, Yuanfeng Ji, Fucang Jia, Ildoo Kim, Klaus Maier-Hein, Dorit Merhof, Akshay Pai, Beomhee Park, Mathias Perslev, Ramin Rezaifar, Oliver Rippel, Ignacio Sarasua, Wei Shen, Jaemin Son, Christian Wachinger, Liansheng Wang, Yan Wang, Yingda Xia, Daguang Xu, Zhanwei Xu, Yefeng Zheng, Amber L. Simpson, Lena Maier-Hein, and M. Jorge Cardoso. The medical segmentation decathlon. *Nature Communications*, 13(1), 2022. 29
- [9] Andre Araujo, Jason Chaves, Haricharan Lakshman, Roland Angst, and Bernd Girod. Large-scale query-by-image video retrieval using bloom filters, 2016. 29
- [10] Guilherme Aresta, Teresa Araújo, Scotty Kwok, Sai Saketh Chennamsetty, Mohammed Safwan, Varghese Alex, Bahram Marami, Marcel Prastawa, Monica Chan, Michael Donovan, et al. Bach: Grand challenge on breast cancer histology images. *Medical image analysis*, 56:122–139, 2019. 7, 20
- [11] S. G. Armato III, G. McLennan, L. Bidaut, M. F. McNitt-Gray, C. R. Meyer, A. P. Reeves, B. Zhao, D. R. Aberle, C. I. Henschke, E. A. Hoffman, E. A. Kazerooni, H. MacMahon, E. J. R. Van Beek, D. Yankelevitz, A. M. Biancardi, P. H. Bland, M. S. Brown, R. M. Engelmann, G. E. Laderach, D. Max, R. C. Pais, D. P. Y. Qing, R. Y. Roberts, A. R. Smith, A. Starkey, P. Batra, P. Caligiuri, A. Farooqi, G. W. Gladish, C. M. Jude, R. F. Munden, I. Petkovska, L. E. Quint, L. H. Schwartz, B. Sundaram, L. E. Dodd, C. Fenimore, D. Gur, N. Petrick, J. Freymann, J. Kirby, B. Hughes, A. V. Castele, S. Gupte, M. Sallam, M. D. Heath, M. H. Kuhn, E. Dharaiya, R. Burns, D. S. Fryd, M. Salganicoff, V. Anand, U. Shreter, S. Vastagh, B. Y. Croft, and L. P. Clarke. Data from lidc-idri, 2015. 29
- [12] Harish Babu Arunachalam, Rashika Mishra, Ovidiu Daescu, Kevin Cederberg, Dinesh Rakheja, Anita Sengupta, David Leonard, Rami Hallac, and Patrick Leavey. Viable and necrotic tumor assessment from whole slide images of osteosarcoma using machine-learning and deep-learning models. *PLoS one*, 14(4):e0210706, 2019. 7, 20
- [13] Muhammad Naseer Bajwa, Gur Amrit Pal Singh, Wolfgang Neumeier, Muhammad Imran Malik, Andreas Dengel, and Sheraz Ahmed. G1020: A benchmark retinal fundus image dataset for computer-aided glaucoma detection. In *2020 International Joint Conference on Neural Networks (IJCNN)*, pages 1–7. IEEE, 2020. 7, 20
- [14] Sven Bambach, Stefan Lee, David J. Crandall, and Chen Yu. Lending a hand: Detecting hands and recognizing activities in complex egocentric interactions. In *The IEEE International Conference on Computer Vision (ICCV)*, 2015. 29
- [15] Sophia Bano, Alessandro Casella, Francisco Vasconcelos, Sara Moccia, George Attilakos, Ruwan Wimalasundera, Anna L. David, Dario Paladini, Jan Deprest, Elena De Momi, Leonardo S. Mattos, and Danail Stoyanov. Fetreg: Placental vessel segmentation and registration in fetoscopy challenge dataset, 2021. 29
- [16] Vivek Singh Bawa, Gurkirt Singh, Francis KapingA, Inna Skarga-Bandurova, Elettra Oleari, Alice Leporini, Carmela Landolfo, Pengfei Zhao, Xi Xiang, Gongning Luo, Kuanquan Wang, Liangzhi Li, Bowen Wang, Shang Zhao, Li Li, Armando Stabile, Francesco Setti, Riccardo Muradore, and Fabio Cuzzolin. The saras endoscopic surgeon action detection (esad) dataset: Challenges and methods, 2021. 29
- [17] Gibran Benitez-Garcia, Jesus Olivares-Mercado, Gabriel Sanchez-Perez, and Keiji Yanai. Ipn hand: A video dataset and benchmark for real-time continuous hand gesture recognition, 2020. 29
- [18] Andrew A Borkowski, Marilyn M Bui, L Brannon Thomas, Catherine P Wilson, Lauren A DeLand, and Stephen M Mastorides. Lung and colon cancer histopathological image dataset (lc25000). *arXiv preprint arXiv:1912.12142*, 2019. 7, 20
- [19] Jannis Born, Nina Wiedemann, Manuel Cossio, Charlotte Buhre, Gabriel Brändle, Konstantin Leidermann, Julie Goulet, Avinash Aujayeb, Michael Moor, Bastian Rieck, and Karsten Borgwardt. Accelerating detection of lung pathologies with explainable ultrasound image analysis. *Applied Sciences*, 11(2), 2021. 29
- [20] David Bouget, Rodrigo Benenson, Mohamed Omran, Laurent Riffaud, Bernt Schiele, and Pierre Jannin. Detecting surgical tools by modelling local appearance and global shape. *IEEE Transactions on Medical Imaging*, 34(12):2603–2617, 2015. 29

- [21] Mathilde Caron, Hugo Touvron, Ishan Misra, Hervé Jégou, Julien Mairal, Piotr Bojanowski, and Armand Joulin. Emerging properties in self-supervised vision transformers. In *Proceedings of the IEEE/CVF international conference on computer vision*, pages 9650–9660, 2021. 1
- [22] Matthias Carstens, Franziska M Rinner, Sebastian Bodenstedt, Alexander C Jenke, Jürgen Weitz, Marius Distler, Stefanie Speidel, and Fiona R Kolbinger. The dresden surgical anatomy dataset for abdominal organ segmentation in surgical data science. *Scientific Data*, 10(1):1–8, 2023. 7, 20
- [23] W. Celniak, M. Wodziński, A. Jurgas, S. Burti, A. Zotti, M. Atzori, H. Müller, and T. Banzato. Improving the classification of veterinary thoracic radiographs through interspecies and inter-pathology self-supervised pre-training of deep learning models. *Sci Rep*, 13(1):19518, 2023. 29
- [24] Tianrun Chen, Lanyun Zhu, Chaotao Ding, Runlong Cao, Yan Wang, Zejian Li, Lingyun Sun, Papa Mao, and Ying Zang. Sam fails to segment anything? – sam-adapter: Adapting sam in underperformed scenes: Camouflage, shadow, medical image segmentation, and more, 2023. 2
- [25] Xuxin Chen, Yuheng Li, Mingzhe Hu, Ella Salari, Xiaoqian Chen, Richard L. J. Qiu, Bin Zheng, and Xiaofeng Yang. Mammo-clip: Leveraging contrastive language-image pre-training (clip) for enhanced breast cancer diagnosis with multi-view mammography, 2024. 3
- [26] Yen-Chun Chen, Linjie Li, Licheng Yu, Ahmed El Kholy, Faisal Ahmed, Zhe Gan, Yu Cheng, and Jingjing Liu. Uniter: Universal image-text representation learning, 2020. 3
- [27] Matthew Christensen, Milos Vukadinovic, Neal Yuan, and David Ouyang. Vision–language foundation model for echocardiogram interpretation. *Nature Medicine*, pages 1–8, 2024. 3
- [28] Noel Codella, Veronica Rotemberg, Philipp Tschandl, M Emre Celebi, Stephen Dusza, David Gutman, Brian Helba, Aadi Kalloo, Konstantinos Liopyris, Michael Marchetti, et al. Skin lesion analysis toward melanoma detection 2018: A challenge hosted by the international skin imaging collaboration (isic). *arXiv preprint arXiv:1902.03368*, 2019. 7, 20
- [29] Paulo Coelho, Ana Pereira, Argentina Leite, Marta Salgado, and António Cunha. A deep learning approach for red lesions detection in video capsule endoscopies. In *Image Analysis and Recognition*, pages 553–561, Cham, 2018. Springer International Publishing. 29
- [30] Chunyan Cui, Li Li, Hongmin Cai, Zhihao Fan, Ling Zhang, Tingting Dan, Jiao Li, and Jinghua Wang. The chinese mammography database (cmmd): An online mammography database with biopsy confirmed types for machine diagnosis of breast, 2021. 29
- [31] Roxana Daneshjou, Kailas Vodrahalli, Roberto A Novoa, Melissa Jenkins, Weixin Liang, Veronica Rotemberg, Justin Ko, Susan M Swetter, Elizabeth E Bailey, Olivier Gevaert, et al. Disparities in dermatology ai performance on a diverse, curated clinical image set. *Science advances*, 8(31): eabq6147, 2022. 7, 20, 29
- [32] Matt Deitke, Christopher Clark, Sangho Lee, Rohun Tripathi, Yue Yang, Jae Sung Park, Mohammadreza Salehi, Niklas Muennighoff, Kyle Lo, Luca Soldaini, Jiasen Lu, Taira Anderson, Erin Bransom, Kiana Ehsani, Huong Ngo, Yen-Sung Chen, Ajay Patel, Mark Yatskar, Chris Callison-Burch, Andrew Head, Rose Hendrix, Favven Bastani, Eli VanderBilt, Nathan Lambert, Yvonne Chou, Arnavi Chheda, Jenna Sparks, Sam Skjonsberg, Michael Schmitz, Aaron Sarnat, Byron Bischoff, Pete Walsh, Chris Newell, Piper Wolters, Tanmay Gupta, Kuo-Hao Zeng, Jon Borchardt, Dirk Groeneveld, Jen Dumas, Crystal Nam, Sophie Lebrecht, Caitlin Wittlif, Carissa Schoenick, Oscar Michel, Ranjay Krishna, Luca Weihs, Noah A. Smith, Hannaneh Hajishirzi, Ross Girshick, Ali Farhadi, and Aniruddha Kembhavi. Molmo and pixmo: Open weights and open data for state-of-the-art multimodal models, 2024. 1
- [33] Karan Desai, Ishan Misra, Justin Johnson, and Laurens van der Maaten. Scaling up instance segmentation using approximately localized phrases. In *British Machine Vision Conference*, 2022. 1, 3
- [34] Alexey Dosovitskiy, Lucas Beyer, Alexander Kolesnikov, Dirk Weissenborn, Xiaohua Zhai, Thomas Unterthiner, Mostafa Dehghani, Matthias Minderer, Georg Heigold, Sylvain Gelly, Jakob Uszkoreit, and Neil Houlsby. An image is worth 16x16 words: Transformers for image recognition at scale. *ICLR*, 2021. 7
- [35] Steven J Durning, John Graner, Anthony R Artino Jr, Louis N Pangaro, Thomas Beckman, Eric Holmboe, Terrence Oakes, Michael Roy, Gerard Riedy, Vincent Capaldi, et al. Using functional neuroimaging combined with a think-aloud protocol to explore clinical reasoning expertise in internal medicine. *Military Medicine*, 177(suppl_9):72–78, 2012. 2
- [36] Sedigheh Eslami, Gerard de Melo, and Christoph Meinel. Does clip benefit visual question answering in the medical domain as much as it does in the general domain? *arXiv preprint arXiv:2112.13906*, 2021. 3, 7
- [37] Jevgenij Gamper and Nasir Rajpoot. Multiple instance captioning: Learning representations from histopathology textbooks and articles. In *Proceedings of the IEEE/CVF conference on computer vision and pattern recognition*, pages 16549–16559, 2021. 3
- [38] Alba García Seco de Herrera, Roger Schaer, Stefano Bromuri, and Henning Müller. Overview of the ImageCLEF 2016 medical task. In *Working Notes of CLEF 2016 (Cross Language Evaluation Forum)*, 2016. 5, 21
- [39] Golnaz Ghiasi, Xiuye Gu, Yin Cui, and Tsung-Yi Lin. Scaling open-vocabulary image segmentation with image-level labels, 2022. 1, 3
- [40] Rohit Girdhar, Alaaeldin El-Nouby, Zhuang Liu, Mannat Singh, Kalyan Vasudev Alwala, Armand Joulin, and Ishan Misra. Imagebind: One embedding space to bind them all. In *Proceedings of the IEEE/CVF Conference on Computer Vision and Pattern Recognition*, pages 15180–15190, 2023. 3
- [41] Shubham Goel. Dermnet. <https://www.kaggle.com/datasets/shubhamgoel27/dermnet>. 29
- [42] Cristina González, Nicolás Ayobi, Isabela Hernández, José Hernández, Jordi Pont-Tuset, and Pablo Arbeláez. Panoptic

- narrative grounding. In *Proceedings of the IEEE/CVF International Conference on Computer Vision (ICCV)*, pages 1364–1373, 2021. 1, 3
- [43] Prof. Shivanand Gornale and Pooja Patravali. Digital knee x-ray images, 2020. 29
- [44] Matthew Groh, Caleb Harris, Luis Soenksen, Felix Lau, Rachel Han, Aerin Kim, Arash Koochek, and Omar Badri. Evaluating deep neural networks trained on clinical images in dermatology with the fitzpatrick 17k dataset, 2021. 29
- [45] Yu Gu, Robert Tinn, Hao Cheng, Michael Lucas, Naoto Usuyama, Xiaodong Liu, Tristan Naumann, Jianfeng Gao, and Hoifung Poon. Domain-specific language model pre-training for biomedical natural language processing, 2020. 7
- [46] Michael Gygli and Vittorio Ferrari. Efficient object annotation via speaking and pointing. *International Journal of Computer Vision*, 128(5):1061–1075, 2020. 1, 4
- [47] Ibrahim Ethem Hamamci, Sezgin Er, Enis Simsar, Atif Emre Yuksel, Sadullah Gultekin, Serife Damla Ozdemir, Kaiyuan Yang, Hongwei Bran Li, Sarthak Pati, Bernd Stadlinger, et al. Dentex: An abnormal tooth detection with dental enumeration and diagnosis benchmark for panoramic x-rays. *arXiv preprint arXiv:2305.19112*, 2023. 29
- [48] Ibrahim Ethem Hamamci, Sezgin Er, Furkan Almas, Ayse Gulnihani Simsek, Sevval Nil Esirgun, Irem Dogan, Muhammed Furkan Dasdelen, Omer Faruk Durugol, Bastian Wittmann, Tamaz Amirashvili, Enis Simsar, Mehmet Simsar, Emine Benu Erdemir, Abdullah Alanbay, Anjany Sekuboyina, Berkan Lafci, Christian Bluethgen, Mehmet Kemal Ozdemir, and Bjoern Menze. Developing generalist foundation models from a multimodal dataset for 3d computed tomography, 2024. 3
- [49] Laura Helle. Prospects and pitfalls in combining eye-tracking data and verbal reports. *Frontline Learning Research*, 5(3):1–12, 2017. 2
- [50] W. Y. Hong, C. L. Kao, Y. H. Kuo, J. R. Wang, W. L. Chang, and C. S. Shih. Cholecseg8k: A semantic segmentation dataset for laparoscopic cholecystectomy based on cholec80, 2020. 29
- [51] Shih-Cheng Huang, Liyue Shen, Matthew P. Lungren, and Serena Yeung. Gloria: A multimodal global-local representation learning framework for label-efficient medical image recognition. In *Proceedings of the IEEE/CVF International Conference on Computer Vision (ICCV)*, pages 3942–3951. IEEE, 2021. 3
- [52] Zhi Huang, Federico Bianchi, Mert Yuksekogul, Thomas Montine, and James Zou. Leveraging medical twitter to build a visual–language foundation model for pathology ai. *bioRxiv*, 2023. 3
- [53] Joni Hyttinen, Pauli Fält, Heli Jäsberg, Arja Kullaa, and Markku Hauta-Kasari. Oral and dental spectral image database—odsi-db. *Applied Sciences*, 10(20), 2020. 29
- [54] Wisdom Ikezogwo, Saygin Seyfioglu, Fatemeh Ghezloo, Dylan Geva, Fatwir Sheikh Mohammed, Pavan Kumar Anand, Ranjay Krishna, and Linda Shapiro. Quilt-1m: One million image-text pairs for histopathology. *Advances in neural information processing systems*, 36, 2024. 3, 4, 5, 7, 18, 21
- [55] Gabriel Ilharco, Mitchell Wortsman, Ross Wightman, Cade Gordon, Nicholas Carlini, Rohan Taori, Achal Dave, Vaishaal Shankar, Hongseok Namkoong, John Miller, Hannaneh Hajishirzi, Ali Farhadi, and Ludwig Schmidt. Openclip, 2021. If you use this software, please cite it as below. 7, 23
- [56] Debesh Jha, Vanshali Sharma, Neethi Dasu, Nikhil Kumar Tomar, Steven Hicks, M. K. Bhuyan, Pradip K. Das, Michael A. Riegler, Pål Halvorsen, Ulas Bagci, and Thomas de Lange. Gastrovision: A multi-class endoscopy image dataset for computer aided gastrointestinal disease detection, 2023. 7, 20
- [57] Chao Jia, Yinfei Yang, Ye Xia, Yi-Ting Chen, Zarana Parekh, Hieu Pham, Quoc Le, Yun-Hsuan Sung, Zhen Li, and Tom Duerig. Scaling up visual and vision-language representation learning with noisy text supervision. In *International conference on machine learning*, pages 4904–4916. PMLR, 2021. 1, 3
- [58] K. V. Jobin, Ajoy Mondal, and C. V. Jawahar. Docfigure: A dataset for scientific document figure classification. *2019 International Conference on Document Analysis and Recognition Workshops (ICDARW)*, 1:74–79, 2019. 29
- [59] Glenn Jocher, Jing Qiu, and Ayush Chaurasia. Ultralytics YOLO, 2023. 5, 21
- [60] Alistair E. W. Johnson, Tom J. Pollard, Seth J. Berkowitz, Nathaniel R. Greenbaum, Matthew P. Lungren, Chih-ying Deng, Roger G. Mark, and Steven Horng. Mimic-cxr, a de-identified publicly available database of chest radiographs with free-text reports. *Scientific Data*, 6(1):317, 2019. 3
- [61] Daniel Kahneman. *Attention and effort*. CiteSeer, 1973. 1
- [62] Z. Karishma. Scientific document figure extraction, clustering and classification, 2021. [32]. 29
- [63] Jakob Nikolas Kather, Niels Halama, and Alexander Marx. 100,000 histological images of human colorectal cancer and healthy tissue. *Zenodo*10, 5281, 2018. 7, 20
- [64] Efklidis Katsaros, Piotr K. Ostrowski, Krzysztof Włodarczyk, Emilia Lewandowska, Jacek Ruminski, Damian Siupka-Mróż, Łukasz Lassmann, Anna Jezierska, and Daniel Węsierski. *Multi-task Video Enhancement for Dental Interventions*, page 177–187. Springer Nature Switzerland, 2022. 29
- [65] Jeremy Kawahara, Sara Daneshvar, Giuseppe Argenziano, and Ghassan Hamarneh. Seven-point checklist and skin lesion classification using multitask multimodal neural nets. *IEEE Journal of Biomedical and Health Informatics*, 23(2): 538–546, 2019. 29
- [66] Aniruddha Kembhavi, Mike Salvato, Eric Kolve, Minjoon Seo, Hannaneh Hajishirzi, and Ali Farhadi. A diagram is worth a dozen images, 2016. 29
- [67] R. Khaled, M. Helal, O. Alfarghaly, O. Mokhtar, A. Elkorary, H. El Kassas, and A. Fahmy. Categorized digital database for low energy and subtracted contrast enhanced spectral mammography images, 2021. 29
- [68] Chanwoo Kim, Soham U Gadgil, Alex J DeGrave, Jesutofunmi A Omiye, Zhuo Ran Cai, Roxana Daneshjou, and Su-In Lee. Transparent medical image ai via an image–text foundation model grounded in medical literature. *Nature Medicine*, pages 1–12, 2024. 3

- [69] Jing Yu Koh, Jason Baldrige, Honglak Lee, and Yinfei Yang. Text-to-image generation grounded by fine-grained user attention. In *Proceedings of the IEEE/CVF Winter Conference on Applications of Computer Vision (WACV)*, pages 237–246, 2021. 1, 3
- [70] Katharina Kriegsmann, Frithjof Lobers, Christiane Zgorzel-ski, Jörg Kriegsmann, Charlotte Janßen, Rolf Rüdinger Meliß, Thomas Muley, Ulrich Sack, Georg Steinbuss, and Mark Kriegsmann. Deep learning for the detection of anatomical tissue structures and neoplasms of the skin on scanned histopathological tissue sections. *Frontiers in Oncology*, 12, 2022. 7, 20
- [71] Ranjay Krishna, Yuke Zhu, Oliver Groth, Justin Johnson, Kenji Hata, Joshua Kravitz, Stephanie Chen, Yannis Kalantidis, Li-Jia Li, David A. Shamma, Michael S. Bernstein, and Fei-Fei Li. Visual genome: Connecting language and vision using crowdsourced dense image annotations, 2016. 1
- [72] Mikhail Kulyabin, Aleksei Zhdanov, Anastasia Nikiforova, Andrey Stepichev, Anna Kuznetsova, Mikhail Ronkin, Vasilii Borisov, Alexander Bogachev, Sergey Korotkich, Paul A. Constable, and Andreas Maier. Octdl: Optical coherence tomography dataset for image-based deep learning methods. *Scientific Data*, 11(1), 2024. 7, 20
- [73] Andreas Leibetseder, Stefan Petscharnig, Manfred Jürgen Primus, Sabrina Kletz, Bernd Münzer, Klaus Schöffmann, and Jörg Keckstein. Lapgyn4: a dataset for 4 automatic content analysis problems in the domain of laparoscopic gynecology. *Proceedings of the 9th ACM Multimedia Systems Conference*, 2018. 29
- [74] Xiujun Li, Xi Yin, Chunyuan Li, Pengchuan Zhang, Xiaowei Hu, Lei Zhang, Lijuan Wang, Houdong Hu, Li Dong, Furu Wei, Yejin Choi, and Jianfeng Gao. Oscar: Object-semantics aligned pre-training for vision-language tasks, 2020. 3
- [75] Stephen Littlefair, Patrick Brennan, Warren Reed, Mark Williams, and Mariusz W Pietrzyk. Does the thinking aloud condition affect the search for pulmonary nodules? In *Medical imaging 2012: image perception, observer performance, and technology assessment*, pages 366–374. SPIE, 2012. 2
- [76] Shilong Liu, Zhaoyang Zeng, Tianhe Ren, Feng Li, Hao Zhang, Jie Yang, Qing Jiang, Chunyuan Li, Jianwei Yang, Hang Su, Jun Zhu, and Lei Zhang. Grounding dino: Marrying dino with grounded pre-training for open-set object detection, 2024. 1
- [77] Ziwei Liu, Ping Luo, Xiaogang Wang, and Xiaoou Tang. Deep learning face attributes in the wild. In *Proceedings of International Conference on Computer Vision (ICCV)*, 2015. 29
- [78] Nathan Louis, Luowei Zhou, Steven J. Yule, Roger D. Dias, Milisa Manojlovich, Francis D. Pagani, Donald S. Likosky, and Jason J. Corso. Temporally guided articulated hand pose tracking in surgical videos, 2021. 29
- [79] Jiasen Lu, Dhruv Batra, Devi Parikh, and Stefan Lee. Vilbert: Pretraining task-agnostic visiolinguistic representations for vision-and-language tasks. In *Advances in Neural Information Processing Systems*. Curran Associates, Inc., 2019. 3
- [80] Xiangde Luo, Wenjun Liao, Jianghong Xiao, Jieneng Chen, Tao Song, Xiaofan Zhang, Kang Li, Dimitris N. Metaxas, Guotai Wang, and Shaoting Zhang. Word: A large scale dataset, benchmark and clinical applicable study for abdominal organ segmentation from ct image. *Medical Image Analysis*, 82:102642, 2022. 29
- [81] Jun Ma, Yuting He, Feifei Li, Lin Han, Chenyu You, and Bo Wang. Segment anything in medical images. *Nature Communications*, 15(1):654, 2024. 2
- [82] Salman Maqbool, Aqsa Riaz, Hasan Sajid, and Osman Hasan. m2caiseq: Semantic segmentation of laparoscopic images using convolutional neural networks. *arXiv preprint arXiv:2008.10134*, 2020. 29
- [83] Xueyan Mei, Zelong Liu, Philip M Robson, Brett Marinelli, Mingqian Huang, Amish Doshi, Adam Jacobi, Chendi Cao, Katherine E Link, Thomas Yang, et al. Radimagenet: an open radiologic deep learning research dataset for effective transfer learning. *Radiology: Artificial Intelligence*, 4(5): e210315, 2022. 7, 20
- [84] Zihang Meng, Licheng Yu, Ning Zhang, Tamara L Berg, Babak Damavandi, Vikas Singh, and Amy Bearman. Connecting what to say with where to look by modeling human attention traces. In *Proceedings of the IEEE/CVF conference on computer vision and pattern recognition*, pages 12679–12688, 2021. 1
- [85] Jesper Molin, Morten Fjeld, Claudia Mello-Thoms, and Claes Lundström. Slide navigation patterns among pathologists with long experience of digital review. *Histopathology*, 67(2):185–192, 2015. 2
- [86] Junya Morita, Kazuhisa Miwa, Takayuki Kitasaka, Kensaku Mori, Yasuhito Suenaga, Shingo Iwano, Mitsuru Ikeda, and Takeo Ishigaki. Interactions of perceptual and conceptual processing: Expertise in medical image diagnosis. *International Journal of Human-Computer Studies*, 66(5):370–390, 2008. 1
- [87] David Morris, Eric Müller-Budack, and Ralph Ewerth. Slideimages: A dataset for educational image classification, 2020. 29
- [88] E. Nagy, M. Janisch, F. Hržić, et al. A pediatric wrist trauma x-ray dataset (grazpedwri-dx) for machine learning. *Sci Data*, 9:222, 2022. 29
- [89] Sahar Almahfouz Nasser, Nihar Gupte, and Amit Sethi. Reverse knowledge distillation: Training a large model using a small one for retinal image matching on limited data, 2023. 29
- [90] National Library of Medicine. Pmc open access subset [internet], 2003. 4, 6, 19
- [91] Ha Q Nguyen, Khanh Lam, Linh T Le, Hieu H Pham, Dat Q Tran, Dung B Nguyen, Dung D Le, Chi M Pham, Hang TT Tong, Diep H Dinh, et al. Vindr-cxr: An open dataset of chest x-rays with radiologist’s annotations. *Scientific Data*, 9(1):429, 2022. 7, 20
- [92] Hieu T Nguyen, Ha Q Nguyen, Hieu H Pham, Khanh Lam, Linh T Le, Minh Dao, and Van Vu. Vindr-mammo: A large-scale benchmark dataset for computer-aided diagnosis in full-field digital mammography. *Scientific Data*, 10(1):277, 2023. 7, 20

- [93] D. Ouyang, B. He, A. Ghorbani, et al. Video-based ai for beat-to-beat assessment of cardiac function. *Nature*, 580: 252–256, 2020. [29](#)
- [94] Samiksha Pachade, Prasanna Porwal, Dhanshree Thulkar, Manesh Kokare, Girish Deshmukh, Vivek Sahasrabudhe, Luca Giancardo, Gwenolé Quéllec, and Fabrice Mériaudeau. Retinal fundus multi-disease image dataset (rfmid): A dataset for multi-disease detection research. *Data*, 6(2), 2021. [29](#)
- [95] Y. Pan, S. Bano, F. Vasconcelos, H. Park, T. T. Jeong, and D. Stoyanov. Desmoke-lap: improved unpaired image-to-image translation for desmoking in laparoscopic surgery. *Int J Comput Assist Radiol Surg*, 17(5):885–893, 2022. [29](#)
- [96] Karen Panetta, Rahul Rajendran, Aruna Ramesh, Shishir Paramathma Rao, and Sos Agaian. Tufts dental database: a multimodal panoramic x-ray dataset for benchmarking diagnostic systems. *IEEE journal of biomedical and health informatics*, 26(4):1650–1659, 2021. [2](#)
- [97] L. Pedraza, C. Vargas, F. Narváez, O. Durán, E. Muñoz, and E. Romero. An open access thyroid ultrasound image database. In *10th International Symposium on Medical Information Processing and Analysis*, pages 188–193. SPIE, 2014. [29](#)
- [98] PKNU-PR-ML-Lab. Calculus. <https://github.com/PKNU-PR-ML-Lab/calculus>. [29](#)
- [99] Konstantin Pogorelov, Kristin Ranheim Randel, Carsten Griwodz, Sigrun Losada Eskeland, Thomas de Lange, Dag Johansen, Concetto Spampinato, Duc-Tien Dang-Nguyen, Mathias Lux, Peter Thelin Schmidt, Michael Riegler, and Pal Halvorsen. Kvasir: A multi-class image dataset for computer aided gastrointestinal disease detection, 2017. [29](#)
- [100] Jordi Pont-Tuset, Jasper Uijlings, Soravit Changpinyo, Radu Soricut, and Vittorio Ferrari. Connecting vision and language with localized narratives, 2020. [1](#), [3](#), [4](#), [6](#)
- [101] Alec Radford, Jeffrey Wu, Rewon Child, David Luan, Dario Amodei, Ilya Sutskever, et al. Language models are unsupervised multitask learners. *OpenAI blog*, 1(8):9, 2019. [7](#)
- [102] Alec Radford, Jong Wook Kim, Chris Hallacy, Aditya Ramesh, Gabriel Goh, Sandhini Agarwal, Girish Sastry, Amanda Askell, Pamela Mishkin, Jack Clark, et al. Learning transferable visual models from natural language supervision. In *International conference on machine learning*, pages 8748–8763. PMLR, 2021. [1](#), [3](#), [6](#), [7](#)
- [103] Alec Radford, Jong Wook Kim, Tao Xu, Greg Brockman, Christine McLeavey, and Ilya Sutskever. Robust speech recognition via large-scale weak supervision. *arXiv preprint arXiv:2212.04356*, 2022. [4](#), [18](#)
- [104] Rubaba Binte Rahman, Sharia Arfin Tanim, Nazia Alfaz, Tahmid Enam Shrestha, M Saef Ullah Miah, and Firoz Mridha. Dental OPG XRAY Dataset, 2024. [7](#), [20](#)
- [105] Pranav Rajpurkar, Jeremy Irvin, Aarti Bagul, Daisy Ding, Tony Duan, Hershel Mehta, Brandon Yang, Kaylie Zhu, Dillon Laird, Robyn L. Ball, Curtis Langlotz, Katie Shpanskaya, Matthew P. Lungren, and Andrew Y. Ng. Mura: Large dataset for abnormality detection in musculoskeletal radiographs, 2018. [29](#)
- [106] J.C.M. Román, V.R. Fretes, C.G. Adorno, R.G. Silva, J.L.V. Noguera, H. Legal-Ayala, J.D. Mello-Román, R.D.E. Torres, and J. Facon. Panoramic dental radiography image enhancement using multiscale mathematical morphology. *Sensors*, 21(9):3110, 2021. [29](#)
- [107] Tobias Ross, Annika Reinke, Peter M. Full, Martin Wagner, Hannes Kennigott, Martin Apitz, Hellena Hempe, Diana Mindroc Filimon, Patrick Scholz, Thuy Nuong Tran, Pierangela Bruno, Pablo Arbeláez, Gui-Bin Bian, Sebastian Bodenstedt, Jon Lindström Bolmgren, Laura Bravo-Sánchez, Hua-Bin Chen, Cristina González, Dong Guo, Pål Halvorsen, Pheng-Ann Heng, Enes Hosgor, Zeng-Guang Hou, Fabian Isensee, Debesh Jha, Tingting Jiang, Yueming Jin, Kadir Kirtac, Sabrina Kletz, Stefan Leger, Zhixuan Li, Klaus H. Maier-Hein, Zhen-Liang Ni, Michael A. Riegler, Klaus Schoeffmann, Ruohua Shi, Stefanie Speidel, Michael Stenzel, Isabell Twick, Gutai Wang, Jiacheng Wang, Lian-sheng Wang, Lu Wang, Yujie Zhang, Yan-Jie Zhou, Lei Zhu, Manuel Wiesenfarth, Annette Kopp-Schneider, Beat P. Müller-Stich, and Lena Maier-Hein. Robust medical instrument segmentation challenge 2019, 2020. [29](#)
- [108] V. Rotemberg, N. Kurtansky, B. Betz-Stablein, L. Caffery, E. Chousakos, N. Codella, M. Combalia, S. Dusza, P. Guitera, D. Gutman, A. Halpern, B. Helba, H. Kittler, K. Kose, S. Langer, K. Lioprys, J. Malvey, S. Musthaq, J. Nanda, O. Reiter, G. Shih, A. Stratigos, P. Tschandl, J. Weber, and P. Soyer. A patient-centric dataset of images and metadata for identifying melanomas using clinical context. *Sci Data*, 8: 34, 2021. [29](#)
- [109] Johannes Rückert, Louise Bloch, Raphael Brüngel, Ahmad Idrissi-Yaghir, Henning Schäfer, Cynthia S Schmidt, Sven Koitka, Obioma Pelka, Asma Ben Abacha, Alba G. Seco de Herrera, et al. Rocov2: Radiology objects in context version 2, an updated multimodal image dataset. *Scientific Data*, 11 (1):688, 2024. [3](#)
- [110] A. Saha, M. R. Harowicz, L. J. Grimm, J. Weng, E. H. Cain, C. E. Kim, S. V. Ghate, R. Walsh, and M. A. Mazurowski. Dynamic contrast-enhanced magnetic resonance images of breast cancer patients with tumor locations (version 3), 2023. [29](#)
- [111] Salman Sajid. Oral diseases. <https://www.kaggle.com/datasets/salmansajid05/oral-diseases>. [29](#)
- [112] Nabeel Sajjad. Dental cavity. <https://www.kaggle.com/datasets/nabeel1921/dental-cavity>. [29](#)
- [113] Joel Saltz, Rajarsi Gupta, Liang Hou, Tahsin Kurc, Parul Singh, Vu Nguyen, Dimitris Samaras, Kenneth R. Shroyer, Ting Zhao, Robert Batiste, Jonathan Van Arnam, The Cancer Genome Atlas Research Network, Ilya Shmulevich, Anirudha U. K. Rao, Alexander J. Lazar, Arvind Sharma, and Vesteinn Thorsson. Tumor-infiltrating lymphocytes maps from tega h&e whole slide pathology images, 2018. Data set. [7](#), [20](#)
- [114] R. Sawyer-Lee, F. Gimenez, A. Hoogi, and D. Rubin. Curated breast imaging subset of digital database for screening mammography (cbis-ddsm), 2016. [29](#)

- [115] Florian Schroff, Dmitry Kalenichenko, and James Philbin. Facenet: A unified embedding for face recognition and clustering. In *Proceedings of the IEEE conference on computer vision and pattern recognition*, pages 815–823, 2015. 5
- [116] Christoph Schuhmann, Romain Beaumont, Richard Vencu, Cade Gordon, Ross Wightman, Mehdi Cherti, Theo Coombes, Aarush Katta, Clayton Mullis, Mitchell Wortsman, Patrick Schramowski, Srivatsa Kundurthy, Katherine Crowson, Ludwig Schmidt, Robert Kaczmarczyk, and Jenia Jitsev. Laion-5b: An open large-scale dataset for training next generation image-text models, 2022. 29
- [117] Christoph Schuhmann, Romain Beaumont, Richard Vencu, Cade W Gordon, Ross Wightman, Mehdi Cherti, Theo Coombes, Aarush Katta, Clayton Mullis, Mitchell Wortsman, Patrick Schramowski, Srivatsa R Kundurthy, Katherine Crowson, Ludwig Schmidt, Robert Kaczmarczyk, and Jenia Jitsev. LAION-5b: An open large-scale dataset for training next generation image-text models. In *Thirty-sixth Conference on Neural Information Processing Systems Datasets and Benchmarks Track*, 2022. 1
- [118] Mehmet Saygin Seyfioglu, Wisdom O Ikezogwo, Fatemeh Ghezloo, Ranjay Krishna, and Linda Shapiro. Quilt-llava: Visual instruction tuning by extracting localized narratives from open-source histopathology videos. In *Proceedings of the IEEE/CVF Conference on Computer Vision and Pattern Recognition*, pages 13183–13192, 2024. 1, 2, 3, 4, 5
- [119] Danli Shi, Weiyi Zhang, Jiancheng Yang, Siyu Huang, Xiaolan Chen, Mayinuer Yusufu, Kai Jin, Shan Lin, Shunming Liu, Qing Zhang, and Mingguang He. Eyeclip: A visual-language foundation model for multi-modal ophthalmic image analysis, 2024. 3
- [120] Amanpreet Singh, Vivek Natarajan, Meet Shah, Yu Jiang, Xinlei Chen, Dhruv Batra, Devi Parikh, and Marcus Rohrbach. Towards vqa models that can read, 2019. 29
- [121] J. Staal, M.D. Abramoff, M. Niemeijer, M.A. Viergever, and B. van Ginneken. Ridge-based vessel segmentation in color images of the retina. *IEEE Transactions on Medical Imaging*, 23(4):501–509, 2004. 29
- [122] Sanjay Subramanian, Lucy Lu Wang, Sachin Mehta, Ben Bogin, Madeleine van Zuylen, Sravanthi Parasa, Sameer Singh, Matt Gardner, and Hannaneh Hajishirzi. Medcat: A dataset of medical images, captions, and textual references, 2020. 5, 21
- [123] Philipp Tschandl, Cliff Rosendahl, and Harald Kittler. The ham10000 dataset, a large collection of multi-source dermatoscopic images of common pigmented skin lesions. *Scientific Data*, 5(1), 2018. 29
- [124] Tao Tu, Shekoofeh Azizi, Danny Driess, Mike Schaeckermann, Mohamed Amin, Pi-Chuan Chang, Andrew Carroll, Charles Lau, Ryutarō Tanno, Ira Ktena, et al. Towards generalist biomedical ai. *NEJM AI*, 1(3):A10a2300138, 2024. 3, 8
- [125] Thomas L. A. van den Heuvel et al. Automated measurement of fetal head circumference using 2d ultrasound images. <https://doi.org/10.5281/zenodo.1327317>, 2018. 29
- [126] A Vaswani. Attention is all you need. *Advances in Neural Information Processing Systems*, 2017. 1
- [127] Bastiaan S Veeling, Jasper Linmans, Jim Winkens, Taco Cohen, and Max Welling. Rotation equivariant cnns for digital pathology. In *Medical Image Computing and Computer Assisted Intervention—MICCAI 2018: 21st International Conference, Granada, Spain, September 16-20, 2018, Proceedings, Part II 11*, pages 210–218. Springer, 2018. 7, 20
- [128] Paul Voigtlaender, Soravit Changpinyo, Jordi Pont-Tuset, Radu Soricut, and Vittorio Ferrari. Connecting Vision and Language with Video Localized Narratives. In *IEEE/CVF Conference on Computer Vision and Pattern Recognition*, 2023. 1, 3, 6
- [129] Paul Voigtlaender, Soravit Changpinyo, Jordi Pont-Tuset, Radu Soricut, and Vittorio Ferrari. Connecting vision and language with video localized narratives. In *Proceedings of the IEEE/CVF Conference on Computer Vision and Pattern Recognition*, pages 2461–2471, 2023. 1
- [130] Xiaosong Wang, Yifan Peng, Le Lu, Zhiyong Lu, Mohammadhadi Bagheri, and Ronald M. Summers. Chestx-ray8: Hospital-scale chest x-ray database and benchmarks on weakly-supervised classification and localization of common thorax diseases. In *2017 IEEE Conference on Computer Vision and Pattern Recognition (CVPR)*, page 3462–3471. IEEE, 2017. 29
- [131] Jerry Wei, Arief Suriawinata, Bing Ren, Xiaoying Liu, Mikhail Lisovsky, Louis Vaickus, Charles Brown, Michael Baker, Naofumi Tomita, Lorenzo Torresani, et al. A petri dish for histopathology image analysis. In *Artificial Intelligence in Medicine: 19th International Conference on Artificial Intelligence in Medicine, AIME 2021, Virtual Event, June 15–18, 2021, Proceedings*, pages 11–24. Springer, 2021. 7, 20
- [132] Ross Wightman. Pytorch image models. <https://github.com/huggingface/pytorch-image-models>, 2019. 7
- [133] Yunfei Xie, Ce Zhou, Lang Gao, Juncheng Wu, Xianhang Li, Hong-Yu Zhou, Sheng Liu, Lei Xing, James Zou, Cihang Xie, and Yuyin Zhou. Medtrinity-25m: A large-scale multi-modal dataset with multigranular annotations for medicine, 2024. 1, 2, 3
- [134] Jiarui Xu, Xingyi Zhou, Shen Yan, Xiuye Gu, Anurag Arnab, Chen Sun, Xiaolong Wang, and Cordelia Schmid. Pixel-aligned language model. In *Proceedings of the IEEE/CVF Conference on Computer Vision and Pattern Recognition*, pages 13030–13039, 2024. 1, 2, 3
- [135] Shivam Yadav. Oral cancer lips and tongue images. <https://www.kaggle.com/datasets/shivam17299/oral-cancer-lips-and-tongue-images>. 29
- [136] Jiahui Yu, Yuanzhong Xu, Jing Yu Koh, Thang Luong, Gunjan Baid, Zirui Wang, Vijay Vasudevan, Alexander Ku, Yinfei Yang, Burcu Karagol Ayan, Ben Hutchinson, Wei Han, Zarana Parekh, Xin Li, Han Zhang, Jason Baldridge, and Yonghui Wu. Scaling autoregressive models for content-rich text-to-image generation. *Transactions on Machine Learning Research*, 2022. Featured Certification. 1, 3
- [137] Jure Zbontar, Florian Knoll, Anuroop Sriram, Tullie Murrell, Zhengnan Huang, Matthew J. Muckley, Aaron Defazio, Ruben Stern, Patricia Johnson, Mary Bruno, Marc

- Parente, Krzysztof J. Geras, Joe Katsnelson, Hersh Chandarana, Zizhao Zhang, Michal Drozdal, Adriana Romero, Michael Rabbat, Pascal Vincent, Nafissa Yakubova, James Pinkerton, Duo Wang, Erich Owens, C. Lawrence Zitnick, Michael P. Recht, Daniel K. Sodickson, and Yvonne W. Lui. fastmri: An open dataset and benchmarks for accelerated mri, 2019. [29](#)
- [138] Haotian Zhang, Pengchuan Zhang, Xiaowei Hu, Yen-Chun Chen, Liunian Li, Xiyang Dai, Lijuan Wang, Lu Yuan, Jenq-Neng Hwang, and Jianfeng Gao. Glipv2: Unifying localization and vision-language understanding. *Advances in Neural Information Processing Systems*, 35:36067–36080, 2022. [1](#)
- [139] Heyu Zhang, Yan He, Xiaomin Wu, Peixiang Huang, Wenkang Qin, Fan Wang, Juxiang Ye, Xirui Huang, Yanfang Liao, Hang Chen, et al. Pathnarratives: Data annotation for pathological human-ai collaborative diagnosis. *Frontiers in Medicine*, 9:1070072, 2023. [1](#), [3](#)
- [140] Sheng Zhang, Yanbo Xu, Naoto Usuyama, Hanwen Xu, Jaspreet Bagga, Robert Tinn, Sam Preston, Rajesh Rao, Mu Wei, Naveen Valluri, et al. Biomedclip: a multimodal biomedical foundation model pretrained from fifteen million scientific image-text pairs. *arXiv preprint arXiv:2303.00915*, 2023. [3](#), [7](#), [8](#)
- [141] Yuhao Zhang, Hang Jiang, Yasuhide Miura, Christopher D Manning, and Curtis P Langlotz. Contrastive learning of medical visual representations from paired images and text. In *Machine Learning for Healthcare Conference*, pages 2–25. PMLR, 2022. [3](#)
- [142] Qi Zhao, Shuchang Lyu, Wenpei Bai, Linghan Cai, Binghao Liu, Guangliang Cheng, Meijing Wu, Xiubo Sang, Min Yang, and Lijiang Chen. Mmotu: A multi-modality ovarian tumor ultrasound image dataset for unsupervised cross-domain semantic segmentation, 2023. [29](#)
- [143] Bolei Zhou, Aditya Khosla, Agata Lapedriza, Antonio Torralba, and Aude Oliva. Places: An image database for deep scene understanding, 2016. [29](#)
- [144] Hong-Yu Zhou, Subathra Adithan, Julián Nicolás Acosta, Eric J Topol, and Pranav Rajpurkar. A generalist learner for multifaceted medical image interpretation. *arXiv preprint arXiv:2405.07988*, 2024. [3](#), [8](#)
- [145] Bin Zhu, Bin Lin, Munan Ning, Yang Yan, Jiayi Cui, Hongfa Wang, Yatian Pang, Wenhao Jiang, Junwu Zhang, Zongwei Li, et al. Languagebind: Extending video-language pretraining to n-modality by language-based semantic alignment. *arXiv preprint arXiv:2310.01852*, 2023. [3](#)

MEDICALNARRATIVES: Connecting Medical Vision and Language with Localized Narratives

Supplementary Material

7. MEDICALNARRATIVES: YouTube Video Curation

Distilling the volume of data YouTube offers into a grounded vision-language dataset that captures the all available signal of medical pedagogy video data is a significant task. Each step in the data curation process presents unique challenges when scaling to handle multiple medical domains.

With MEDICALNARRATIVES, we collect vision-language datasets grounded in time with language-correlated traces across twelve medical domains with the first three domains defined to be *static* where representative samples are usually static images: (1) computed tomography (CT), (2) magnetic resonance imaging (MRI), and (3) xray, and *non-static* domain with representative samples exhibiting significant visual change: (4) ultrasound, (5) surgery, (6) endoscopy, (7) dentistry, (8) dermatology, (9) mammography, (10) ophthalmology, (11) histopathology and (12) general medical illustrations. When processing these subsets, our approach differs to accommodate the nuances of the video data. Our data curation pipeline can be split into these high-level tasks of:

- (A) Searching for representative videos in each medical domain.
- (B) Filtering videos for narrative style.
- (C) Extracting image, text, and cursor traces from selected videos.
- (D) Denoising and de-duplicating the collected raw data.
- (E) Aligning image, text, and localization traces.
- (F) Collecting metadata useful for varying downstream tasks (e.g. subdomains) and interleaving the dataset.

In the following sections, we present a detailed overview of the major steps in curating MEDICALNARRATIVES starting with search. We also present examples of curated narrative samples in Figures 5, 6, 7, and 8.

7.1. Domain-Specific Search

We first identify medical channels and videos for each domain on YouTube, using keywords from online medical glossaries specific to each imaging modality or medical domain. To increase the percentage of narrative or educational style videos, a list of priority keywords: "educational", "interpretation", "case study", and similar phrases, are appended to search keywords. We limit our search to channels with <1M subscribers since some channels focus on multiple domains (e.g. radiology channels span CT, MRI, X-ray) and therefore might have a large subscriber base, and channels with >1M

subscribers often contain non-imaging videos.

We observe during channel search that searching YouTube for channels by keyword tends to produce irrelevant results, hence, we adopt a video-first search strategy: since video titles are more informative than channel titles, we first find relevant videos, then evaluate the channel of the relevant video for more hits. Each video result is downloaded in low resolution for further analysis. To limit searching irrelevant channels we implement early stopping, wherein, if the first 10 videos of a channel fail the medical filtering step, the channel is skipped, allowing us to keep compute cost low while increasing our pool of visited channels.

7.2. Medical Filtering

Each potential pedagogy video is evaluated by the following heuristics:

1. The video duration is longer than 1 minute and shorter than 2 hours as videos outside this range usually contain little medical imaging information.
2. Video contains speech. We check this either through the video's transcript from the YouTube API, or if not present using the `inaSpeechSegmenter`² tool on the first minute of audio.
3. The number of medical scene frames exceeds the empirically determined threshold unique to each medical domain. This heuristic filters for narrative-style videos (See Section 7.3).

To expand on the third heuristic, we extract the keyframes of a video for classification; for static domains, we utilize `FFmpeg`³ to detect scenes and extract keyframes (frames with significant visual changes from previous frames). We experiment with scene detection thresholds to determine the optimal threshold per domain across various video durations. For non-static domains, we leverage adaptive content scene detection in⁴ to avoid capturing frames that are visually different but still part of the same shot (which are characteristic of non-static domains). Camera movements are common in domains such as surgery or endoscopy, and nearly duplicate frames that would be generated by thresholding on video content are instead merged when using `PySceneDetect`'s adaptive detection algorithm. We specifically tune the adaptive detection for each domain by experimentally determining parameters for the algorithm on sample videos from each domain.

²<https://github.com/ina-foss/inaSpeechSegmenter>

³<https://github.com/FFmpeg/FFmpeg>

⁴<https://github.com/Breakthrough/PySceneDetect>

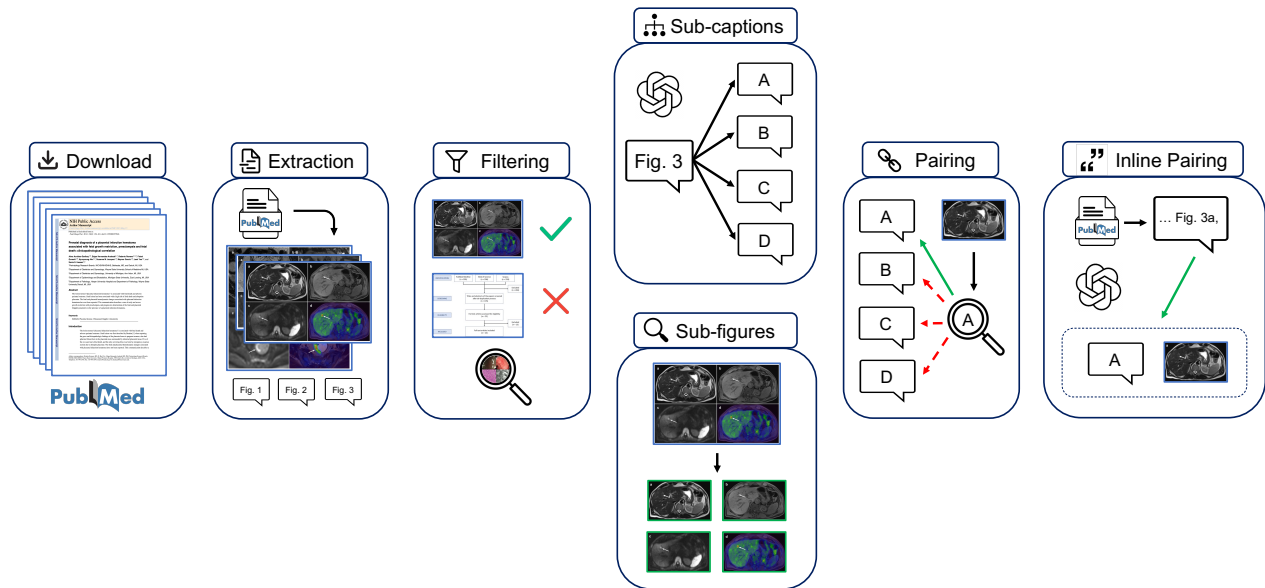


Figure 4. The data curation pipeline for the PubMed subset of the MEDICALNARRATIVES dataset. **Download**: downloading PMC-OA. **Extraction**: extracting figures, captions, and inline references. **Filtering**: filtering for medical images. **Sub-captions**: splitting compound figure captions into sub-captions. **Sub-figures**: detecting and cropping sub-figures from compound figures. **Pairing**: matching sub-figures and sub-captions. **Inline pairing**: matching inline mentions of figures with the most relevant sub-figure or sub-captions.

We then classify the key-frames of a video using pre-trained classifiers per domain (see Section 10.3). Using the percentage of key-frames predicted to be medical images, videos are differentiated into three categories: positive videos, near-positive videos, and negative videos. For example, a video with 50% of key-frames predicted to be MRI images is a candidate for further processing, while a video with only 2% of key-frames is not. Positive videos contain sufficient medical content for the given domain, while near-positive videos may or may not contain sufficient medical content. The thresholds defining positive/near-positive/negative are unique to each domain. We then manually examine a subset of the near-positive category, and determine a more fine-grained percentage threshold to extract more positive videos out of the pool of near-positive videos. See Table 3 for the final percentage thresholds used.

7.3. Narrative Filtering

We define narrative-style videos as pedagogy videos where the narrator focuses on describing or analyzing medical images onscreen. To filter for these videos, we first check the first minute of each medical video for speech using inaspeechsegmenter to ascertain the presence of a narrator.

For static domains like X-ray, we define a narrative streak as any partition of the video where frames sampled close (w.r.t. time) together are similar using cosine similarity,

Domain	Threshold (%)
CT & X-ray	10
MRI	5
Dermatology & Dentistry	30
Endoscopy & Surgery	50
Ultrasound	40
Ophthalmology	35
Mammography	25
General medical illus.	20

Table 3. Final percentage thresholds used during video key-frame classification.

indicating the narrator is spending a lot of time analyzing that frame. Specifically, we randomly sample a fixed number of clips across each video, sampling three consecutive frames from each clip and checking for similarity. Finally, if the number of streaks in each video is greater or equal to the set threshold for that domain, the video is considered to be narrative. This simple filtering algorithm helps us reduce the number of videos we process from 748k to 74k videos.

For non-static domains like surgery or ultrasound, consecutive key-frames often exhibit significant change so we instead look for persistent narration around key-frames classified as medical. For example, for ultrasound clips, we extract the times for each consecutive positive key-frame accumulating a sequence of start and end times. Within these

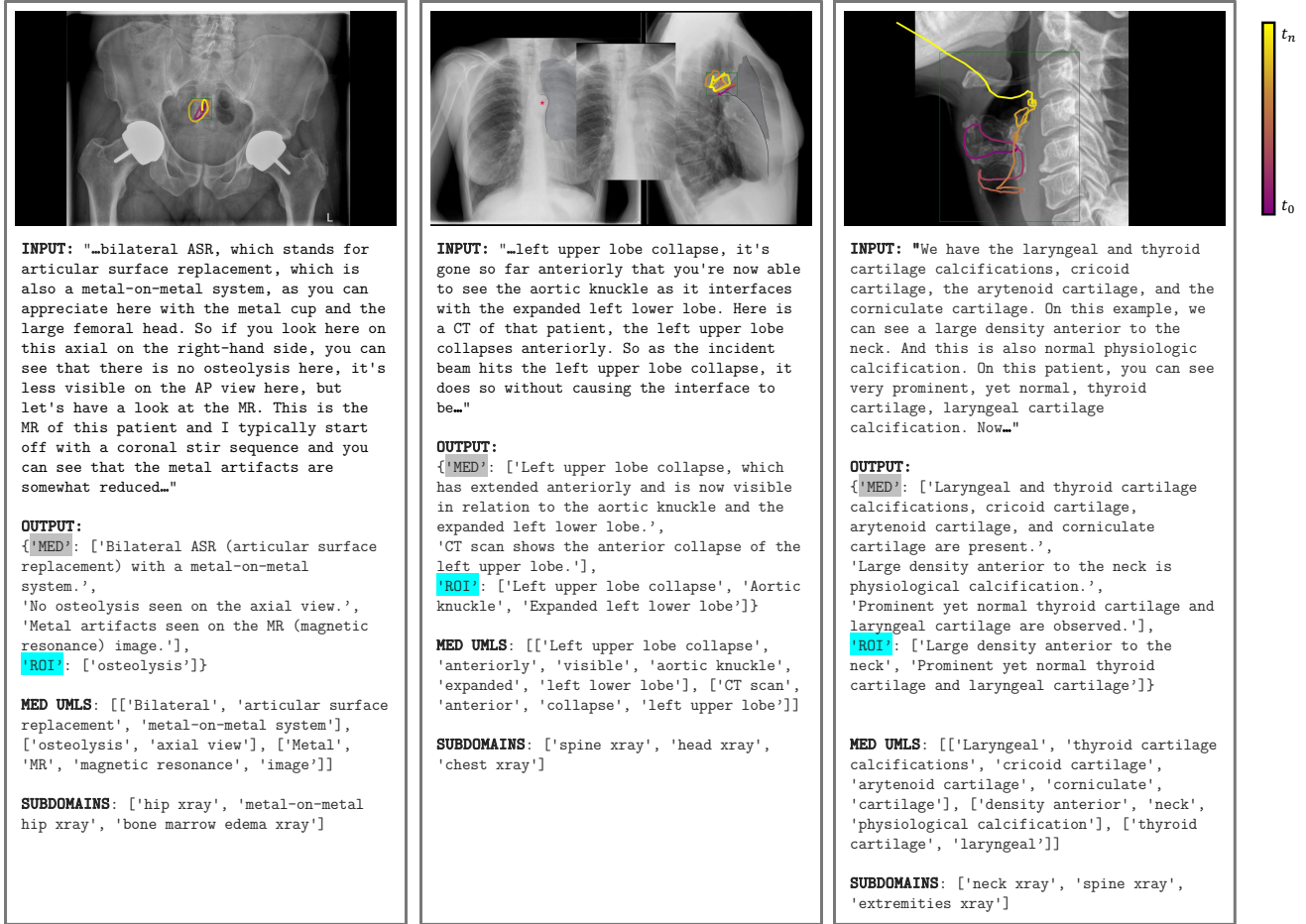


Figure 5. **X-ray examples** within the MEDICALNARRATIVES dataset. **Input:** raw input text from ASR. **Output:** the output from the LLM, with denoised medical and ROI text. **Traces:** Cursor traces and bounding boxes aligned in-time with the raw text. **UMLS:** UMLS entities extracted from the medical text. **Subdomain:** classification of the sample into finer-grained subdomains.

time intervals, we determine whether speech exists either through the video’s YouTube API transcript or by extracting the audio during the selected time interval and using inaSpeechSegmenter to determine if the segment contains any speech.

7.4. Text Extraction using ASR and Text Denoising.

In line with Quilt-1M [54] we leverage an open-source ASR model - Whisper [103] to transcribe all speech from the selected videos and make sure to account for transcription errors using a similar methodology of finding these types of errors and correcting with a language model. We use the whisper-large-v2 model in the stable-ts library for word-level and sentence-level transcription. As anticipated, this model often misinterprets medical terms, thus requiring the use of post-processing algorithms to minimize its error rates. For this, we adopt a similar methodology proposed in Quilt-1M [54] to identify, correct, and verify these errors, please see

section A.1 in Quilt-1M [54] supplementary for more details.

From the ASR-corrected text, we extract *medical text* which describes the image(s) as a whole. Also, when the speaker describes/gestures at visual regions-of-interest through statements like "look here ...", we extract the text entity being described as *ROI text* in line with Quilt-1M [54].

To extract relevant text, we prompt LLMs to filter out all non-medically relevant text, providing context as necessary, while conditioning the LLMs to refrain from introducing new words beyond the corrected noisy text and set the model’s temperature to zero. Lastly, the LLM is used to categorize our videos into subdomains by conditioning with a few examples and prompting with the corrected video transcript as input (see Figure 11 for prompt and sample input/output).

7.5. Identifying Cross-Modality Samples

To aid in interleaving the dataset we find videos with multiple medical modalities by leveraging a language model

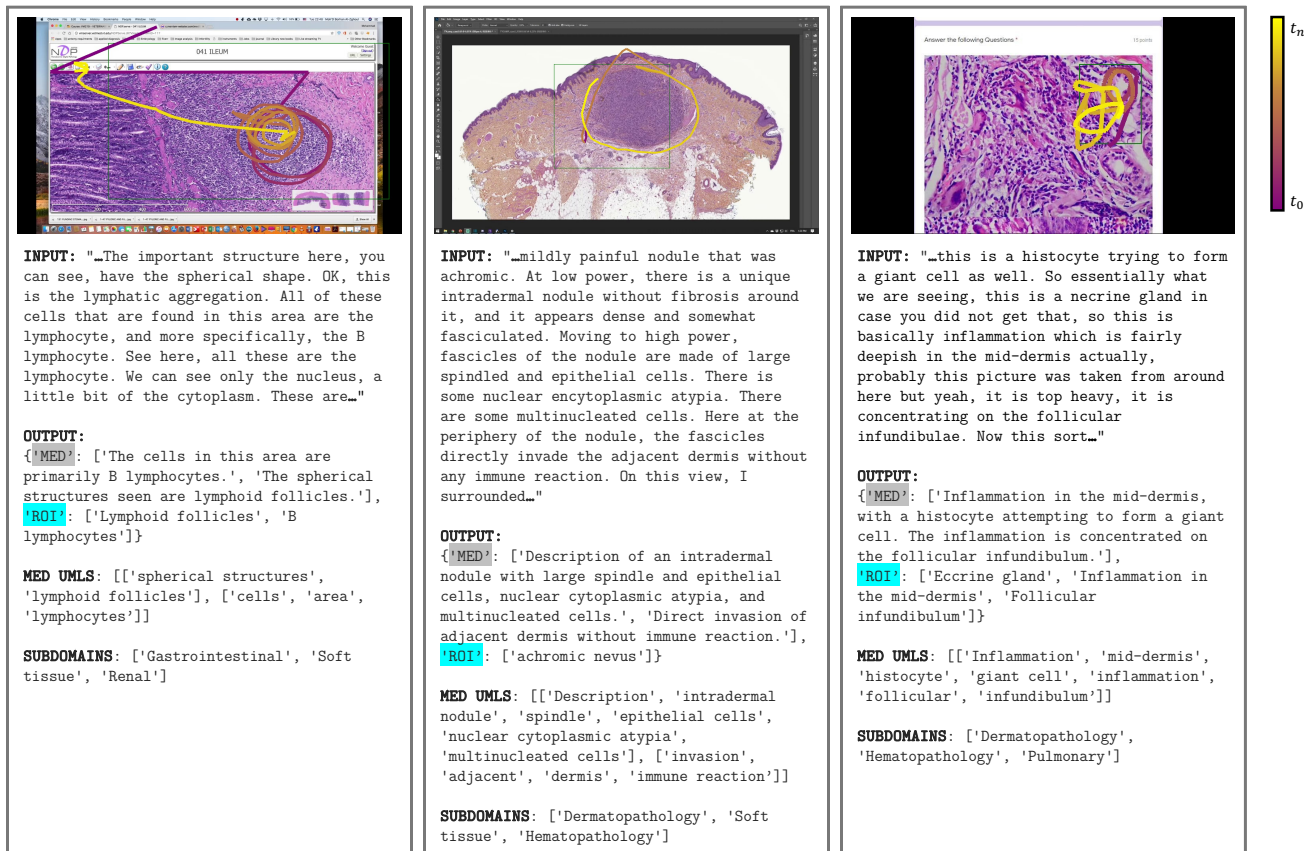


Figure 6. **Histopathology examples** within the MEDICALNARRATIVES dataset. **Input:** raw input text from ASR. **Output:** the output from the LLM, with denoised medical and ROI text. **Traces:** Cursor traces and bounding boxes aligned in-time with the raw text. **UMLS:** UMLS entities extracted from the medical text. **Subdomain:** classification of the sample into finer-grained subdomains.

Hyperparameter	Training
Batch size (per GPU)	256
Epochs	20
Peak learning rate	1e-5
Learning rate schedule	cosine decay
Warmup (in steps)	2000
Augmentation	Resize; RandomCrop (0.8, 1.0)
Optimizer momentum	$\beta_1, \beta_2 = 0.9, 0.98$
Weight decay	0.2
Optimizer	AdamW

Table 4. Training hyperparameters for GENMEDCLIP

Hyperparameter	ResNet50	ViT-Small
Batch size (per GPU)	256	32
Epochs	10	100
Peak learning rate	1e-2	1e-3
Learning rate schedule	-	cosine annealing
Augmentation	RandomResizedCrop (224), Resize	RandomResizedCrop (384, 0.98, 1.0), RandomHorizontalFlip
Optimizer momentum	0.9	0.9
Weight decay	1e-4	-
Optimizer	SGD	SGD

Table 5. Training hyperparameters for domain classifiers.

8. MEDICALNARRATIVES: PubMed Article Curation

conditioned with a prompt with a list of all relevant medical modalities, the transcript of the video, 3 human-curated examples, prompting the model to output the list of modalities that are relevant to the transcript given (see Figure 10). Finally, we run the respective domain classifiers on each of the representative images in the video to determine which images (samples) are relevant to each identified domain.

To curate the PubMed subset of MEDICALNARRATIVES, we download the PubMed Central Open Access Subset (PMCOA) [90], containing 5.47 million articles and filter article figures for the same twelve domains as the YouTube subset of MEDICALNARRATIVES. Our data curation pipeline for PubMed is as follows:

Datasets	prompt
Pcam [127], Nck [63], Lc2500 [18], Mhist [131]	["a histopathology slide showing {c}.", "histopathology image of {c}.", "pathology tissue showing {c}.", "presence of {c} tissue on image"]
Bach [10], Skin [70], Osteo [12]	
Tcga_til [113], DDI [31], Isic [28], Dental [104]	["{c} presented in image", "evidence of {c} in image", "an image showing {c}"]
Gastrovision [56], G1020 [13], Octdl [72], VinDrM [92] VinDrXR [91], Dresden [22], Radimagenet [83]	

Table 6. Zero-shot classification templates used to evaluate GENMEDCLIP’s zero-shot capacity across all multiple dataset that constitute the medical benchmark.

Models	Xray (mAP)	CT		MRI					Mammo (mAP)	US	Optha	Derm	Endo	Surg	Dental	Histo										Overall				
	vindrXR	lung	abd	af	brain	hip	knee	abd	shdr	spine	vindrM	rad	g1020	octdl	ddi	isic	gastro	dresden	dental	til	pcam	lc	lung	nck	skin		skin_tumor	lc_colon	mhist	bach
CLIP-ViT-B-32	6.95	2.74	4.14	2.75	0.77	2.67	1.86	2.23	3.13	12.29	10.64	8.45	69.61	10.22	41.31	21.76	4.94	10.66	-	21.33	61.81	61.55	29.20	4.47	9.84	65.57	50.67	25.25	58.85	21.63
CLIP-ViT-B-16	6.55	1.61	3.76	3.59	6.55	3.00	1.13	1.49	4.29	14.07	10.65	5.41	31.47	6.98	60.67	13.23	1.77	11.38	2.51	20.32	51.80	47.06	21.41	5.55	13.22	79.56	52.61	23.75	43.54	18.93
PUBMEDCLIP	7.40	6.06	2.04	1.08	8.95	1.38	4.07	0.54	8.50	31.21	10.45	15.94	68.33	7.56	35.52	18.19	2.05	9.72	12.19	24.55	50.38	33.33	26.45	8.07	23.01	63.66	62.74	15.25	43.63	20.77
BIOMEDCLIP	10.29	6.80	2.53	3.11	12.31	2.98	4.88	0.97	6.09	11.35	10.57	58.10	29.12	18.60	51.22	20.70	3.49	16.37	16.83	37.03	71.71	71.34	49.17	24.83	40.39	84.98	38.59	44.25	46.75	27.43
GENMEDCLIP-32	10.23	14.25	1.59	2.25	23.40	3.68	9.45	1.18	2.36	24.00	10.30	44.98	66.67	20.35	62.96	19.78	2.10	15.04	26.89	23.14	70.56	81.11	48.05	28.45	49.67	93.24	55.37	37.25	55.82	31.18
GENMEDCLIP-PMB	9.90	10.36	2.30	3.95	8.80	1.80	4.33	0.98	8.38	25.04	12.06	52.98	29.22	24.56	57.01	37.63	2.08	19.30	16.83	49.63	71.90	82.05	51.05	39.32	48.34	71.68	61.82	52.00	42.44	30.96
GENMEDCLIP	9.66	27.35	1.38	2.75	7.52	2.61	9.93	2.80	3.10	22.59	11.12	63.48	33.53	21.22	72.26	37.10	2.38	18.97	16.44	20.34	65.90	72.37	52.16	42.37	59.87	94.16	60.59	52.50	41.43	31.99

Table 7. **Expanded Zeroshot Classification Results** shows that our model GENMEDCLIP outperforms all other baselines including the out-of-domain CLIP and biomedical vision-language models BIOMEDCLIP and PUBMEDCLIP across the constructed medical benchmark. The benchmark covers all 11 medical domains represented, excluding the non-medical domain of medical illustrations. The metric for X-ray and Mammography is mean average precision while the rest is accuracy.

Domain	CT	MRI	X-ray
Image-text-ROI pairs	34224	41019	32241
Image-text-ROI-text pairs	51041	54213	49639
Avg. ROI Text/Image ROI	3.29	2.9	3.82
Num. ROI Text/Video	96771.0	84409.0	85682.0
Avg. Words/ROI Text	10.65	9.61	12.32
Avg. ROI UMLS/Text	1.47	1.48	1.47
Avg. ROI/Image	1.61	1.38	1.74
Avg. ROI Text/Chunk	2.61	2.33	2.54
Unique ROI BBox	45465	34709	49208
Unique ROI Traces	11386480	4744770	10650027
Avg. ROI Chunk Duration	12.94	6.23	14.39
Avg. BBox Height	321.7	205.1	312.44
Avg. Bbox Width	543.12	282.65	507.58

Table 8. Characterization of MEDICALNARRATIVES *image-text-trace* subset, categorized by individual medical domains. The table provides detailed statistics for each medical modality, including the number of unique images, total dataset duration, ASR error rate, and average image resolution. Note: "ROI" in the table is shorthand for traces.

- Downloading PMC-OA and extracting each article’s XML and images.
- Parsing each XML to extract figure captions and inline mentions of figures.
- Filtering for figures with medical imaging with pre-trained classifiers.
- Splitting compounded figures and captions using fine-tuned object detection models and a language model.
- Pairing correctly split sub-captions and sub-figures together using a combination of optical character recog-

nition (OCR), bounding box heuristics, and error correction.

- Matching inline mentions of figures with sub-figure/sub-caption pairs using a language model.

In the following sections, we will discuss the MEDICAL-NARRATIVES PubMed data pipeline.

8.1. Caption Extraction

From each obtained PubMed article, we extract the XML and image files for figure processing. The figure captions are extracted from the paper XML, cleaned, and paired with the corresponding image file of the figure. Additionally, we find all inline mentions of the figure and save them to the figure-caption sample. This yields 23.6M figure-caption samples.

8.2. Medical Filtering

To determine whether a figure belongs to one of the twelve domains of MEDICALNARRATIVES, we train a ResNet-50 CNN for binary classification. We use the same training datasets (see Table 10) selected when curating MEDICAL-NARRATIVES YouTube data, with a binary medical/non-medical label as the target prediction. This filtering step reduces the number of potential figures to 1.03M figures. To determine the specific domain or domains of each figure, we re-use the medical domain classifiers from the medical filtering step.

8.3. Sub-figure Detection

The majority of figures after medical filtering are compound figures, which compress detailed information into a single image and caption. Splitting these compound figures into sub-figures is a non-trivial task, since there is no uniform compound figure layout. In contrast to Quilt-1M’s [54] image processing-based approach to splitting these figures, we opt for an object detection approach, which we empirically determined is capable of handling wider range of abstract layouts.

Specifically, we finetune a YOLO object detection model [59] to detect sub-figures within compound figures using two medical subfigure separation datasets: MedICaT’s sub-figure annotations and ImageCLEF 2016’s Figure Separation medical task [38, 122]. MedICaT contains 7507 sub-figure bounding box annotations from 2069 compound figures. ImageCLEF 2016 Figure Separation contains 6782 sub-figure bounding box annotations. We fine-tune a YOLOv8-Large [59] for 100 epochs using an 80/20 training/validation split on the subfigure separation data. One major advantage of the object detection approach is that our model can successfully detect sub-figures even when there is little to no gap/whitespace in-between sub-figures. We process each figure with the fine-tuned YOLOv8 sub-figure detection model, where each detected sub-figure is cropped, and up-scaled by a factor of 4. In the case of compounded figures with uncompounded caption i.e. all constituting images communicate a singular concept (see Figure 9) we pair the caption to the original compounded figure.

8.4. Sub-caption Separation

A compound figure caption usually contains multiple sub-captions. A heuristics-based approach to splitting these compounded captions is difficult to design since figure sub-captions are labeled differently with article authors adhering to varying writing styles typically set by the publishing journal. We therefore opt for an LLM-based approach where we provide diverse examples of sub-caption separation, instructing the language model (GPT-3.5 Turbo) to follow the process below:

1. Separate the figure caption into sub-captions based on the sub-figure labels present in the caption e.g. "(A)", "I)", "a.", "bottom left", etc.
2. Strip the sub-figure labels from each sub-caption text produced.
3. If any context in the caption pertains to the entire figure, add this context to each sub-caption. This step ensures that each individual sub-caption retains the entire context of the figure.
4. Return each sub-caption paired with its sub-figure label.

We condition the LLM with a few examples, including handling non-compound figures and captions that use spa-

tial cues (e.g. left, center, right) to refer to sub-figures (see full prompt and sample input/output in Figure 12). We also process the sub-figure labels returned from the LLM, stripping parentheses and other extraneous characters to make sub-figure/sub-caption pairing easier.

8.5. Pairing Sub-figures to Sub-captions

Given the separated sub-captions and sub-figures for a compound figure, next we tackle the problem of pairing the correct sub-caption with the correct subfigure. The majority of our curated PubMed data uses alphabetic labels in compound figures to denote sub-figures. Our approach therefore leverages optical character recognition on each sub-figure to detect the sub-figure labels, which we then match to the sub-caption labels extracted during section 8.4.

During the sub-figure detection step, we upscale the detected sub-figures by a factor of 4 to enlarge the sub-figure text label for OCR. We impose a 95% confidence threshold on predicted text during OCR to isolate the sub-figure label. Text detected at lower confidence is often other text in the figure (e.g. axis titles, graphs) being present. We then attempt to match the detected sub-figure label with the sub-caption label. If a match is found, we pair the selected sub-figure and sub-caption.

There are several types of cases where this approach requires error handling, e.g.:

1. In a single sub-figure, no labels are identified that exceed the 95% confidence threshold.
2. Sub-captions use spatial cues to identify sub-figures, e.g. "upper left", "center", "right".
3. If the number of detected sub-figures does not match the number of sub-captions: either some sub-figures or some sub-captions are unpaired.

In case 1, if the compound figure has exactly one sub-figure and one sub-caption left unpaired, we pair the two. Otherwise, we lower the confidence threshold to 80% and re-detect sub-figure labels, then re-match with sub-captions. Sub-figures that fall in this category tend to have their label close to the border of the cropped sub-figure, have small sub-figure text, or have backgrounds that resemble the font color of the label. For case 2, we use the bounding box coordinates of the detected sub-figures and the spatial cues provided in the caption to pair figures and captions. For example, a sub-caption with the label "upper left" will be paired with the sub-figure with the upper leftmost bounding box. Lastly, case 3 occurs when either sub-figure detection and/or sub-caption separation perform incorrectly. The majority of figures in this category occur when sub-figure detection identifies multiple sub-figures, but the figure caption contains no sub-captions. In this case, we pair the original figure and caption.

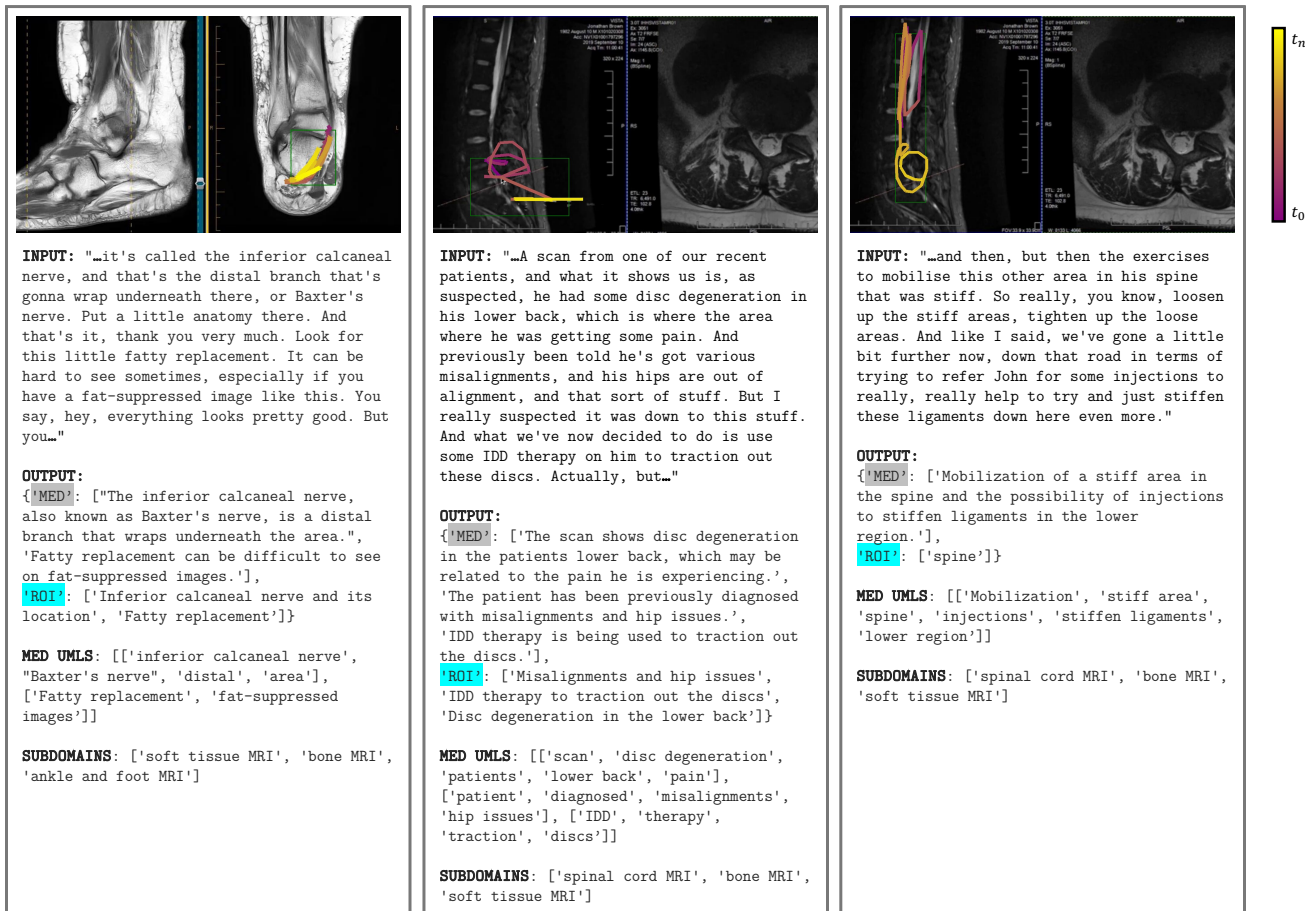


Figure 7. **MRI examples** with in the MEDICALNARRATIVES dataset. **Input:** raw input text from ASR. **Output:** the output from the LLM, with denoised medical and ROI text. **Traces:** Cursor traces and bounding boxes aligned in-time with the raw text. **UMLS:** UMLS entities extracted from the medical text. **Subdomain:** classification of the sample into finer-grained subdomains.

Domain	CT	MRI	Endo	Genmed	Surgery	Optha	Mammo	Derma	Ultrasound	X-ray	Dentist
Unique images	45889	54093	43230	23836	74435	758	288	19627	39084	54714	15369
Image-text pairs	37648	47211	40027	20318	64567	284	42	12057	31138	42521	11552
Total Med UMLS	290143	254279	504753	222699	649566	3243	251	106291	319199	270256	57086
Avg. Med Text/Image	2.44	2.14	3.49	2.79	2.85	2.48	1.4	2.02	2.69	2.56	2.54
Num. Med Text/Video	78931	70733	134385	54251	183259	681	59	26904	83768	17194	14867
Avg. Words/Med Text	28.38	24.03	40.3	36.03	32.1	36.74	15.62	23.49	31.64	30.07	30.61
Avg. Med UMLS/Text	3.75	3.68	3.83	4.28	3.57	6.07	4.25	3.89	3.93	3.83	3.87
Total Chunks	40883	38462	42770	23800	73314	758	283	19420	38948	37056	7655
Avg. Chunk Duration	31.33	18.36	47.08	36.4	28.83	74.6	2.42	23.6	31.33	34.05	50.38
Avg. Med Text/Chunk	2.13	1.97	3.23	2.35	2.48	1.27	0.16	1.0	2.08	2.07	1.7
Avg. Images/Chunk	1.25	1.52	1.01	1.0	1.04	1.0	1.02	1.01	1.0	1.75	2.04
Avg. Image-Text/Chunk	1.07	1.26	0.93	0.83	0.88	0.49	0.12	0.47	0.76	1.33	1.23
Precision (Unconditioned)	0.16	0.15	0.18	0.17	0.18	0.2	0.33	0.23	0.16	0.19	0.2
Precision (Conditioned)	0.48	0.45	0.48	0.56	0.54	0.44	0.73	0.43	0.41	0.46	0.42
Clinical ASR Error Rate	0.01	0.01	0.01	0.01	0.01	0.01	0.01	0.01	0.01	0.01	0.01
Total Duration (hrs)	324.0	410.0	428.0	278.0	383.0	15.0	0.0	187.0	735.0	562.0	140.0
Avg. Duration (mins)	13.31	12.04	6.24	9.72	7.58	6.94	0.11	8.06	12.43	19.22	13.69
Total ASR len. (words)	2342164	3314197	2721970	2061495	2933993	89011	4399	1203913	6245504	4485366	1149694
Avg. ASR len. (words)	1602.03	1619.05	660.99	1198.54	965.45	659.34	879.8	863.64	1759.3	2555.76	1872.47
Avg. Image Width	1530.82	1243.16	1302.91	1582.66	1707.22	988.71	1496.0	1717.6	1582.51	1491.5	1831.86
Avg. Image Height	954.37	789.68	759.47	1026.71	995.96	627.85	1128.0	998.99	910.32	923.71	1045.61

Table 9. Characterization of MEDICALNARRATIVES *image-text* subset, categorized by individual medical domains. The figure provides detailed statistics for each medical modality, including the number of unique images, total dataset duration, ASR error rate, and average image resolution.

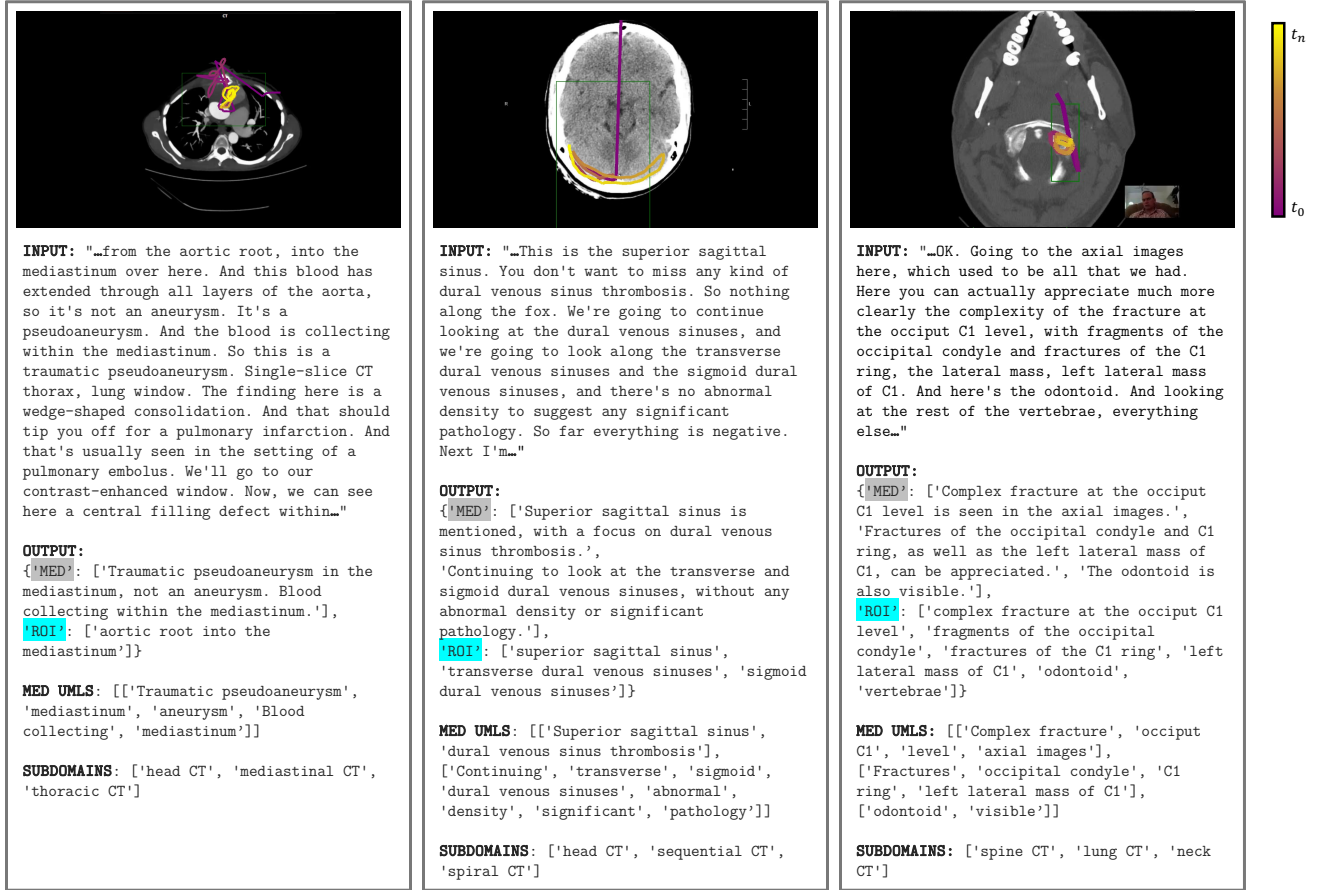


Figure 8. CT examples with in the MEDICALNARRATIVES dataset. **Input:** raw input text from ASR. **Output:** the output from the LLM, with denoised medical and ROI text. **Traces:** Cursor traces and bounding boxes aligned in-time with the raw text. **UMLS:** UMLS entities extracted from the medical text. **Subdomain:** classification of the sample into finer-grained subdomains.

8.6. Inline Figure Reference Pairing

In the final step of the pipeline, we pair the inline reference of a figure with the figure caption since inline references contain valuable context about the figure. However, an inline reference may refer to a sub-figure instead of the entire figure. We therefore utilize a language model to determine which sub-figure is most relevant to an inline reference. For each sample, we prompt an LLM (GPT-3.5 Turbo) with the list of sub-figure labels and a list of inline references and task the model with determining which sub-figure label best corresponds to the inline reference. In the case that the reference cites the entire figure instead of a sub-figure, we consider the inline reference relevant to all sub-figures. For each relevant sub-figure, we add the inline reference to its list of captions. See Figure 13 for the complete prompt and sample input/output.

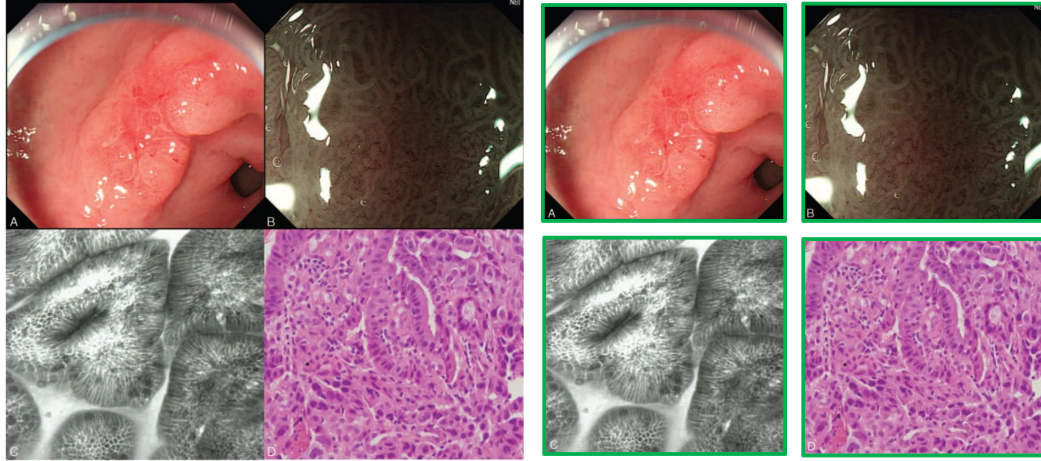
9. Characterizing MEDICALNARRATIVES

To create MEDICALNARRATIVES we combine medical narratives curated from videos with image-text pairs curated from PubMed, resulting in 4.7M total image-text samples of which 1M samples are localized narratives. Section 3.4 gives an overview characterization of the entire dataset, and Tables 9, 8 below provide additional specific characterization details split per domain. Note we omit characterization for Histopathology in the tables below as the details for the domain can be found in prior work.

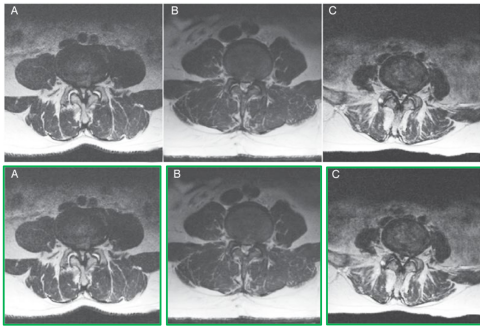
10. Model Training and Evaluation

10.1. GENMEDCLIP Training

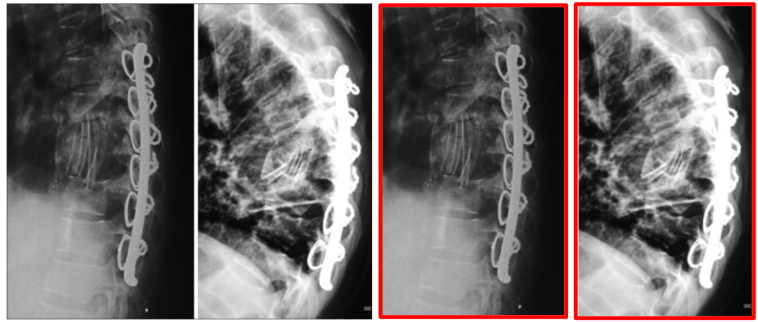
We leverage OpenCLIP [55] to train our models as it allows us to quickly import our datasets and adapt varying components of our model including the underlying image and text towers and the training hyperparameters. Our experiments utilize Pytorch on 4 NVIDIA L40s GPUs, as well as gradient



(a)



(b)



(c)

Figure 9. (a), (b) Compound figures successfully separated into sub-figures (green), which are then up-scaled and saved. (c) A figure that is incorrectly identified as a compound figure. Since the figure caption contains no sub-captions, the original figure will be paired with the entire caption during sub-figure/sub-caption pairing.

checkpointing, automatic mixed precision with bfloat16 to reduce memory usage. All other hyperparameters used are listed in Table 4. Our dataset is split into 16 tar files in the WebDataset⁵ format for training.

10.2. Evaluation

To evaluate zero-shot classification capacity across all constituting datasets in our medical benchmark outlined in 4 we leverage simple prompts listed in Table 6, with the specific results shown in Table 7.

10.3. Search Classifiers

To classify images into domains, we train a ResNet50 for 10 epochs and a ViT-Small for 100 epochs using DINO on a binary classification task for each medical domain. Both types of models are trained on 4 NVIDIA A4000 GPUs. All hyperparameters are listed in Table 5. For each classifier, we use domain-specific datasets as positive samples and non-medical datasets as negative samples. For the binary


medical/non-medical classifier used in Section 8.2, we use all medical domain datasets as positive samples, and the same group of non-medical datasets as negative samples. See Table 10 for an overview of the datasets used to train these classifiers.

⁵<https://github.com/webdataset/webdataset>

System Prompt: `Imagine you are a text classifier. Classify the given text into the given types.`

User Prompt: `Imagine you are a text classifier. Classify the given text into the following types: X-ray, MRI, CT, ultrasound, endoscopy, surgery, dermatology, dentistry, mammography, ophthalmology, general medical. Output only the relevant types in an ordered python list.`

Few-shot examples: `"Scanning from the right upper quadrant to the right lower quadrant. Acute right lower quadrant pain. Gallbladder and hyperechoic area. The clinical examination shows the external, internal obliques, and the transversus abdominis muscles. The presence of the hyperechoic area may indicate fat stranding or fat edema, which can be seen in appendicitis. Fat stranding or fat edema is sometimes seen in appendicitis, but the appendix in this case was normal. Color-doppler image shows no flow within the fat. Color-doppler image shows no flow within the fat. Hyperechoic fat is seen in case number two, with a bit of edema. Iliac vessels can be seen in the clip. Hyperechoic, hyperechoic fat that appears edematous. Identification of iliac vessels (artery and vein), right ovary. Iliac artery and iliac vein. Hyperechoic, edematous fat. Right ovary. Abdominal CT scan in axial plane."`
`"['ultrasound', 'ct']"`

 **INPUT:** `"Case 52 shows the strength of hydrogen bonding. The third case is an aminotasis and the third case is a natural hemangioma. The learning point is that natural hemangioma appears very large and uniform in all three recipes. The third case is impossible to be a hemangioma and the third is a hydatid cyst. The weak area is the hemangioma. In this equal image of the three infections, we see a large hemangioma with a central lamp. Despite the rest of the hemangioma, which is a group of internal recipes containing blood.. The doctor also has brain notes. Possible notes of carcinoma or hepatocellular notes. We have an old CT brain note and this is a brain note and the correct answer is metastasis because we have a normal note sign here. Increase in size of hepatocellular carcinoma over a period of 6 years. The learning point is that hepatocellular carcinoma can significantly increase in size over time."`

OUTPUT: `"['ct', 'ultrasound', 'mri']"`

Figure 10. The GPT-3.5 Turbo prompts used to determine whether a video contains discussion of multiple medical domains, with few-shot examples.

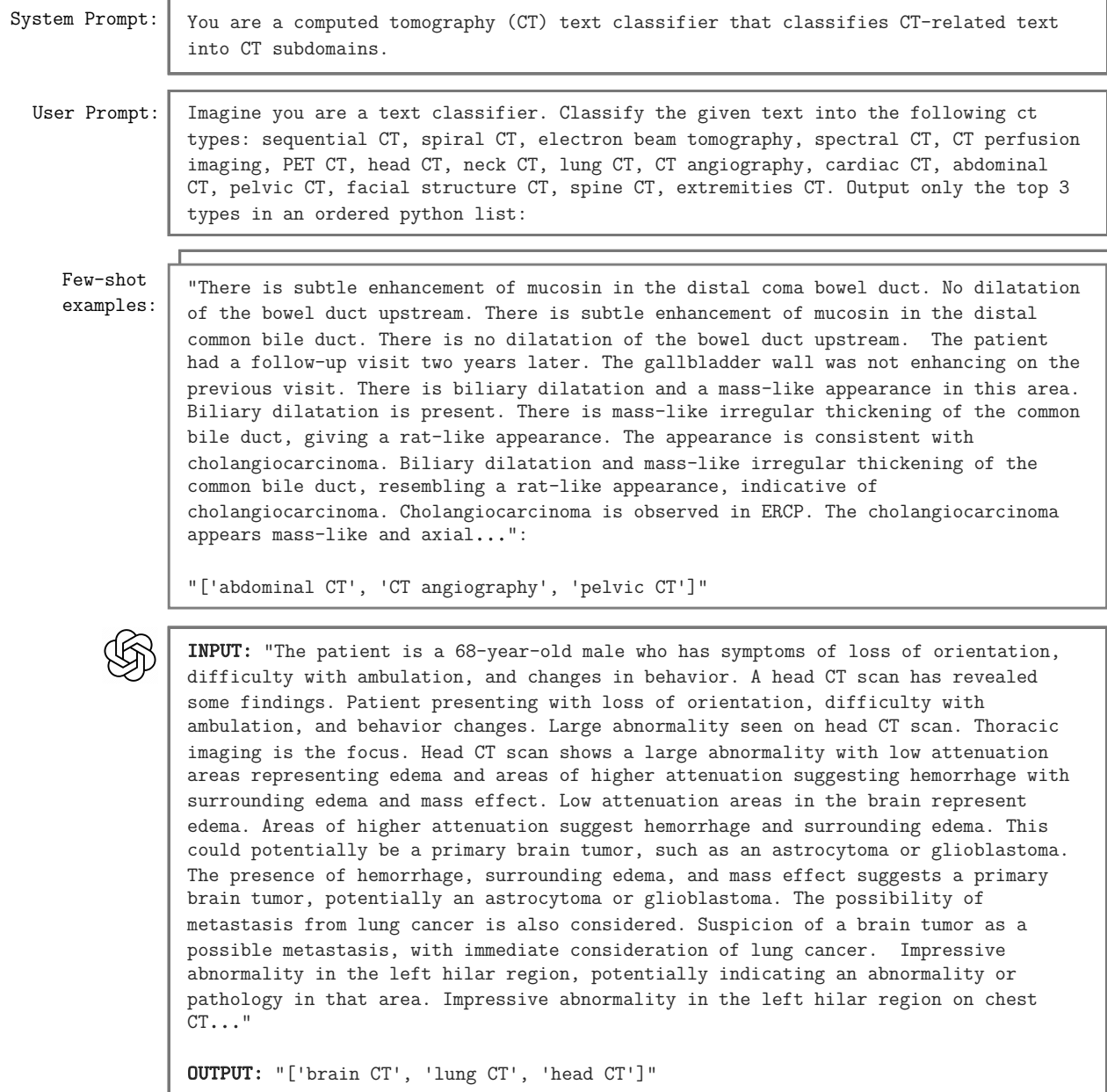


Figure 11. The GPT-3.5 Turbo prompts used for determining which specific sub-domains are discussed in a video, with few-shot examples.

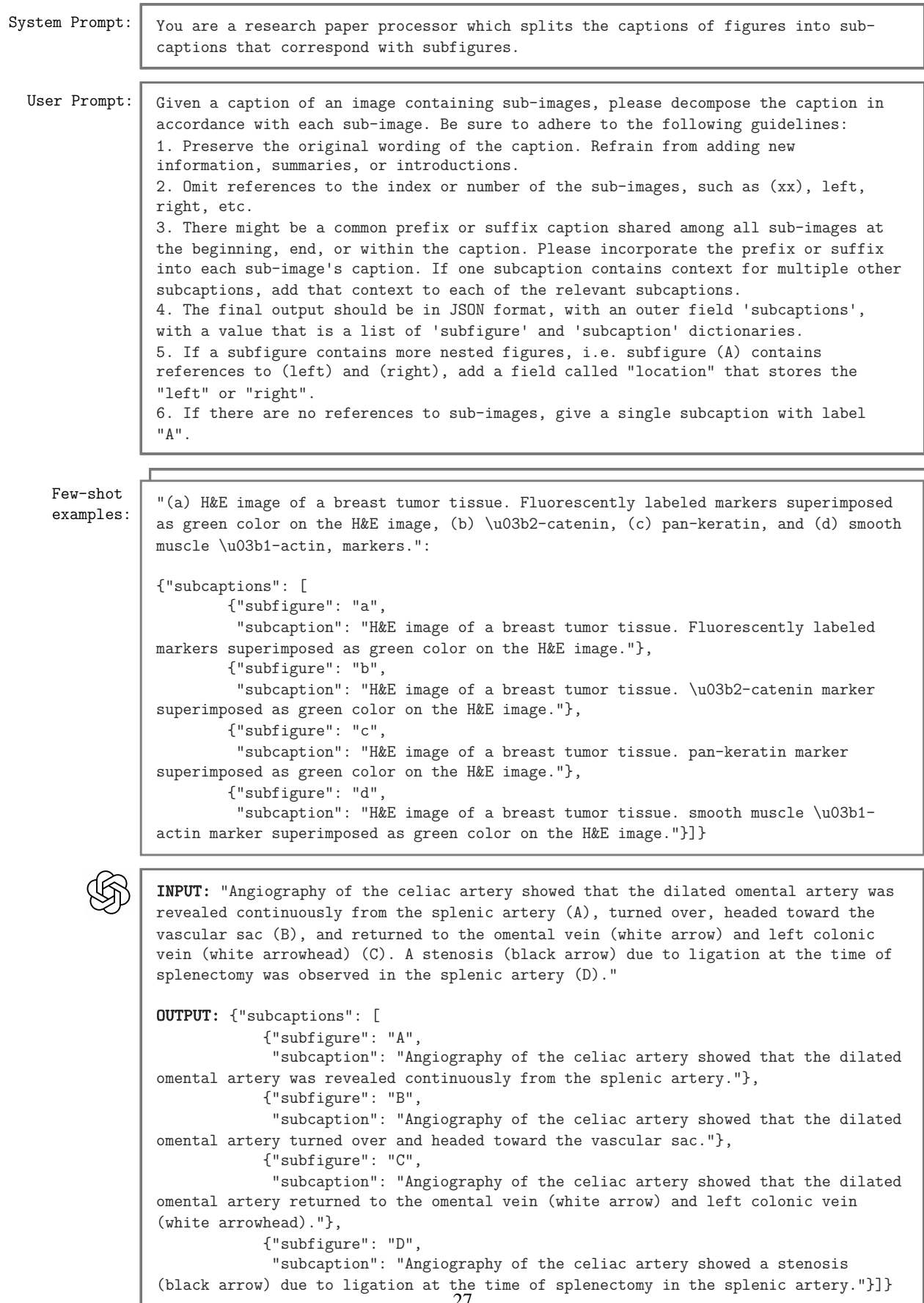


Figure 12. The GPT-3.5 Turbo prompts used for splitting a compound figure caption into sub-captions, with few-shot examples.

System Prompt: You are a research paper processor which splits the captions of figures into sub-captions that correspond with subfigures.

User Prompt: You are given the sub-figures and sub-captions of a figure in a medical article. You are also given the inline mentions of the figure. Return a JSON where each inline mention is paired to the most relevant subfigure, and all strings in the JSONs have double quotes. If the inline mentions are broadly applicable to all subcaptions, add the inline mentions to each subcaption. If the inline mentions aren't applicable to any subcaption, return an empty JSON.


Few-shot examples:

```

{"img_inline_sentences": ["As shown in Figure 7, lithium-treatment caused marked decrease in the mean protein abundance of NKCC2 in the renal medulla of WT mice.",
    "9-fold higher protein abundance as compared to the WT mice (Figure 7B).",
    "In contrast, in the cortex lithium administration caused significant decreases in NKCC2 protein abundance in both WT and KO mice with no difference in their mean values (Figure 7D).",
    "Interestingly, similar to AQP2 protein abundance, the mean NKCC2 protein abundance in control diet-fed P2Y2 KO mice was 2-fold higher as compared to the corresponding value in WT mice (Figure 7D)."],
    "subcaptions": ["A", "B", "C", "D"]}:

{"A": ["As shown in Figure 7, lithium-treatment caused marked decrease in the mean protein abundance of NKCC2 in the renal medulla of WT mice."],
    "B": ["As shown in Figure 7, lithium-treatment caused marked decrease in the mean protein abundance of NKCC2 in the renal medulla of WT mice.", "9-fold higher protein abundance as compared to the WT mice (Figure 7B)."],
    "C": ["As shown in Figure 7, lithium-treatment caused marked decrease in the mean protein abundance of NKCC2 in the renal medulla of WT mice."],
    "D": ["As shown in Figure 7, lithium-treatment caused marked decrease in the mean protein abundance of NKCC2 in the renal medulla of WT mice.", "In contrast, in the cortex lithium administration caused significant decreases in NKCC2 protein abundance in both WT and KO mice with no difference in their mean values (Figure 7D).", "Interestingly, similar to AQP2 protein abundance, the mean NKCC2 protein abundance in control diet-fed P2Y2 KO mice was 2-fold higher as compared to the corresponding value in WT mice (Figure 7D)."]}

```

 **INPUT:**

```

{"img_inline_sentences": ["The mass demonstrated a scattered calcification and expansive bony destruction (Fig 2)."],
    "subcaptions": ["A", "B"]}

```

OUTPUT:

```

{"A": ["The mass demonstrated a scattered calcification and expansive bony destruction (Fig 2)."],
    "B": ["The mass demonstrated a scattered calcification and expansive bony destruction (Fig 2)."]}

```

Figure 13. The GPT-3.5 Turbo prompts used for pairing inline references of a figure with the most relevant sub-figures, with few-shot examples.

Domain	Dataset	Total samples	Train	Test	Image Size
CT	LIDC-IDRI [11]	10005	7004	3002	512 × 512
	TCGA-LUAD [5]	48931	34252	14679	512 × 512
	WORD [80]	30495	21347	9149	512 × 512
X-ray	Positive Videos	1612	1128	484	
	ChestX-ray14 [130]	112120	78484	33636	1024 × 1024
	GRAZPEDWRI-DX [88]	20327	14229	6098	660 × 1660
	Shoulder X-ray Classification [23]	841	589	252	
	Digital Knee X-ray [43]	1650	1155	495	300 × 162
	MURA [105]	40561	28393	12168	1500 × 2000
MRI	Positive Videos	692	484	208	1440 × 1080
	fastMRI [137]	58847	41193	17654	320 × 320
	Duke-Breast-Cancer-MRI [110]	922	645	277	256 × 256
	Medical Segmentation Decathlon [8]	2633	1843	790	256 × 256
Dermatology	Positive Videos	118	83	35	
	Dermnet [41]	19500	13650	5850	720 × 472
	DDI [31]	656	459	197	300 × 300
	7-point [65]	2045	1432	614	480 × 720
	ISIC [108]	33126	23188	9938	
Endoscopy	Fitzpatrick 17k [44]	16577	11604	4973	
	HAM10000 [123]	10015	7011	3005	800 × 600
	KVASIR [99]	8000	5600	2400	720 × 576
	ITEC LapGyn4 [73]	59439	41607	17832	256 × 256
	Red Lesion Endoscopy [29]	3895	2727	1169	320 × 320
	FetReg [15]	12334	8634	3700	
US	TMEDOM [7]	956	669	287	
	Positive Videos	9496	6647	2849	
	COVID-19 Ultrasound [19]	59	41	18	
	BUSI [4]	780	546	234	500 × 500
	DDTI [97]	134	94	40	560 × 360
	MMOTU [142]	1639	1147	492	330888 × 218657
Dentistry	HC18 [125]	1334	934	400	
	EchoNet-Dynamic [93]	10030	7021	3009	112 × 112
	Positive Videos	1874	1312	562	
	Panoramic radiography [106]	598	419	179	2041 × 1024
	ODSI-DB [53]	316	221	95	
	DENTEX 2023 [47]	2332	1632	700	
	Dental Calculus [98]	220	154	66	
	Vident-lab [64]	15110	10577	4533	416 × 320
	Dental condition [111]	1296	907	389	612 × 408
	Oral cancer [135]	144	101	43	
Surg	Dental cavity [112]	176	123	53	
	SARAS-ESAD [16]	27175	19023	8153	1920 × 1080
	CholecSeg8k [50]	8080	5656	2424	854 × 480
	DeSmoke-LAP [95]	6000	4200	1800	
	Surgical Hands [78]	2838	1987	851	
	m2caiSeg [82]	307	215	92	716 × 402
Optha	NeuroSurgicalTools [20]	2476	1733	743	612 × 460
	ROBUST-MIS 2019 [107]	10000	7000	3000	960 × 540
	Cataracts [6]	35127	24589	10538	1920 × 1080
	Ocular Disease Recognition [2]	3358	2351	1007	512 × 512
	MeDAL Retina [89]	2181	1527	654	768 × 768
	RFMID [94]	3200	2240	960	2144 × 1424
Mammo	Glaucoma Detection [1]	650	455	195	3072 × 2048
	DRIVE [121]	40	28	12	584 × 565
	CBIS-DDSM [114]	10239	7167	3072	
Genmed Non-medical	CDD-CESM [67]	2006	1404	602	2355x1315
	CMMD [30]	5202	3641	1561	
	LAION [116]	10861	7603	3258	
	Celeb [77]	202599	60780	28364	178 × 218
	Places [143]	10624928	637496	399497	200 × 200
	A12D [66]	4903	3432	1471	
	DocFig [58]	33028	26422	6606	
	SciFig-Pilot [62]	263952	211162	52790	
	SlideImages [87]	3452	2762	690	
	TextVQA [120]	25119	20095	5024	
Non-medical	SlideShare-1M [9]	977605	782084	195521	
	Negative Videos	23956	19165	4791	
	EgoHands [14]	4800	3840	960	720 × 1080
	11k Hands [3]	11076	8861	2215	1600 × 1200
	IPN Hand [17]	95021	76017	19004	640 × 480

Table 10. Datasets used to train ResNet50 and ViT-Small medical image classifiers, used in Section 7.2 and Section 8.2.